Elasticity-inspired data-driven micromechanics theory for unidirectional composites with interfacial damage

Qiang Chen[a], Wenqiong Tu[b], Jiajun Wu [c*], Zhelong He[d], George Chatzigeorgiou[e], Fodil Meraghni[e], Zhibo Yang[a], Xuefeng Chen[a]

[a] School of Mechanical Engineering, Xi'an Jiaotong University, Xi'an 710049, Shaanxi, China

[b] School of Automotive and Traffic Engineering, Jiangsu University, Zhenjiang 212013, China

[c] Arts et Métiers Institute of Technology, PIMM, HESAM University, F-75013 Paris, France

[d] State Key Laboratory of Advanced Design and Manufacturing for Vehicle Body, College of Mechanical and Vehicle Engineering, Hunan University, Changsha 410082, China

[e] Arts et Métiers Institute of Technology, CNRS, Université de Lorraine, LEM3-UMR7239, F-57000 Metz, France

* Corresponding author: jiajun.wu@ensam.eu

Abstract

We present a novel elasticity-inspired data-driven Fourier homogenization network (FHN) theory for periodic heterogeneous microstructures with square or hexagonal arrays of cylindrical fibers. Towards this end, two custom-tailored networks are harnessed to construct microscopic displacement functions in each phase of composite materials, based on the exact Fourier series solutions of Navier's displacement differential equations. The fiber and matrix networks are seamlessly connected through a common loss function by enforcing the continuity conditions, in conjunction with periodicity boundary conditions, of both tractions and displacements. These conditions are evaluated on a set of weighted collocation points located on the fiber/matrix interface and the exterior faces of the unit cell, respectively. The partial derivatives of displacements are computed effortlessly through the automatic differentiation functionality. During the training of the FHN model, the total loss function is minimized with respect to the Fourier series parameters using gradient descent and concurrently maximized with respect to the

adaptive weights using gradient ascent. The transfer learning technique is employed to speed up the training of new geometries by leveraging a pre-trained model. Comparison with finite-element/volume-based unit cell solutions under various loading scenarios showcases the computational capability of the proposed method. The utility of the proposed technique is further demonstrated by capturing the interfacial debonding in unidirectional composites via a cohesive interface model.

Keywords: Physically informed machine learning; Micromechanics; Composites; Interface damage; Fourier series; Elasticity

1. Introduction

The myriad combinations of constituent phases and microstructures in heterogeneous materials have motivated extensive developments of micromechanics methodologies in the past fifty years. These methods, in general, can be separated into two categories according to their distinct geometric representations of underlying microstructures (Pindera et al., 2009): I) representative volume element (RVE) based methods in the analysis of statistically homogeneous composites (Christensen and Lo, 1979; Hashin and Rosen, 1964; Mori and Tanaka, 1973); II) repeating unit cell (RUC) based methods in the analysis of periodic composites (Chen et al., 2018; Cruz-González et al., 2020; Praud et al., 2020; Tu and Chen, 2020b). In most cases, the RVE-based techniques provide closed-form expressions for the averaged or homogenized moduli with sufficient accuracy, hence they continue to be utilized in the composite micromechanics communities. However, one notable limitation of these approaches is that they often fail to provide an accurate estimation of the local stress concentration within each phase owing to the simple geometric representation of underlying microstructures of the composites.

The need to account for the intricate adjacent fiber interactions observed in real microstructures has thus contributed to the greater emphasis on the development of unit cell approaches that require sophisticated analytical or numerical treatments (Chen et al., 2018; Drago and Pindera, 2007; El Fallaki Idrissi et al., 2024). The latter replies on periodic boundary conditions of both surface displacements and tractions, hence the response of an RUC, i.e., the smallest element of periodic microstructures, is identical to that of the materials at large. The majority of the periodic homogenization methods depend on the numerical solutions of the unit cell boundary value problem, such as the finite-element or finite-volume-based techniques (Cavalcante and Pindera, 2016; Chen et al., 2018; Cruz-González et al., 2020; Praud et al., 2020; Tu and Chen, 2020b). Conversely, the exact elasticity-based solution for unit cell problems is not commonly found in the literature because of the inherent challenges in satisfying both displacement and traction periodicity conditions simultaneously. An exception is the locally exact homogenization theory developed by Pindera and his coworkers (Drago and Pindera, 2008; He and Pindera, 2020; Wang and Pindera, 2016) over the past decade. In this technique, the Fourier series are utilized to represent the displacement fields that exactly fulfill Navier's displacement equations while the periodicity boundary conditions of displacements and tractions are imposed by an efficient but rather complicated balanced variational principle.

Over the past five years, the physics-informed neural network (PINN) has emerged as an attractive alternative to the conventional analytical or numerical methods for solving coupled partial differential equations with specified spatio-temporal boundary conditions (Haghighat et al., 2021; Huang et al., 2022; Raissi et al., 2019; Samaniego et al., 2020; Vahab et al., 2022). In this model, the neural network is trained on a set of collocation points to obtain the optimized network parameters (weights and biases) by minimizing a loss function composed of residuals of the

governing partial differential equations and the relevant spatio-temporal boundary conditions (Raissi et al., 2019). The automatic differentiation of the modern machine-learning library is typically exploited to construct the loss function, offering an additional advantage.

PINN has been harnessed in the micromechanical modelling of heterogeneous materials by several investigators with various degrees of success. Much work in the open literature has focused on the implementation of boundary conditions, a fundamental but nontrivial task for PINN solutions of unit cell problems. The commonly utilized penalty method introduces a penalty coefficient to each boundary loss, whereas the penalty coefficients are determined from a trial-and-error approach. The network can easily fail to train due to the competing effects with multiple loss terms (Dong and Ni, 2021). In response to this limitation, Henkes et al. (2022) employed modified neural network outputs to enforce the Dirichlet displacement boundary and Neumann traction boundary conditions. Promising results have been demonstrated in their work. However, only limited loading conditions have been considered and the predicted displacements and stresses do not strictly obey the periodicity constraints as required by the homogenization theory due to the difficulty of constructing the modified network outputs that adhere strictly to periodicity boundary conditions. A deep homogenization framework for unidirectional composites with general loading conditions has been also proposed by the present authors (Jiang et al., 2023; Wu et al., 2023). This new framework introduces a periodic layer by using sinusoidal functions (Dong and Ni, 2021) that exactly enforce the periodicity displacements with arbitrary prescribed periods in 2D or 3D space to infinite orders. A limitation of the DHN method is that it relies on one single neural network to approximate the entire unit cell solutions for the fiber/matrix phases. As a result, the neural network predicted displacement fields are infinitely differentiable due to the chosen activation function. However, in heterogeneous materials, the displacement field does not fulfill C^{∞} continuity.

Therefore, training the DHN network faces substantial difficulty in the vicinity of the fiber/matrix interface where significant deformation/stress gradients are encountered.

In this contribution, we aim to construct a novel elasticity-inspired data-driven micromechanics model for unidirectional composites with square or hexagonal arrays of transversely isotropic phases. Following the zeroth-order homogenization framework, the displacement fields can be decomposed into averaged and fluctuating components dependent on the global and microscopic scales. In the context of the PINN technique, we represent the fluctuating displacements in the fiber and matrix domains using two custom-tailored network models derived from the elasticity solutions of Navier's displacement equations, c.f., Pindera and his coworkers (Drago and Pindera, 2008; Wang and Pindera, 2016), respectively. The fiber and matrix displacement networks are seamlessly related by imposing the traction and displacement continuity conditions at the fiber/matrix interface on a set of weighted collocation points in the overall loss function. Furthermore, we apply traction and displacement periodicity boundary conditions to the matrix network at a separate set of weighted collocation points. The strains are evaluated effortlessly with the help of automatic differentiation in PyTorch library, which substantially simplifies setting up the network model. To overcome the difficulty in training networks with multiple loss terms, we attempt to minimize the total loss function with regard to the Fourier series parameters based on the gradient descent, but concurrently maximize the total loss function about the adaptive weights based on the gradient ascent. Transfer learning is explored to speed up the training for new geometries based on the network that has been already trained once. The full potential of the FHN framework has been demonstrated upon the incorporation of the cohesive zone model for simulating the interfacial debonding in unidirectional composites.

2. Theoretical framework

2.1 Unit cell problem overview

Let us consider periodic arrays of cylindrical fibers aligned along the x_1 axis in the matrix phase, as shown in Figure 1, which can be represented by a repeating unit cell that defines the material's microstructures. The displacement fields $\mathbf{u}^{(q)}$ in each phase can be expressed in terms of two-scale expansion involving macro- and microscopic contributions as follows (Du et al., 2024):

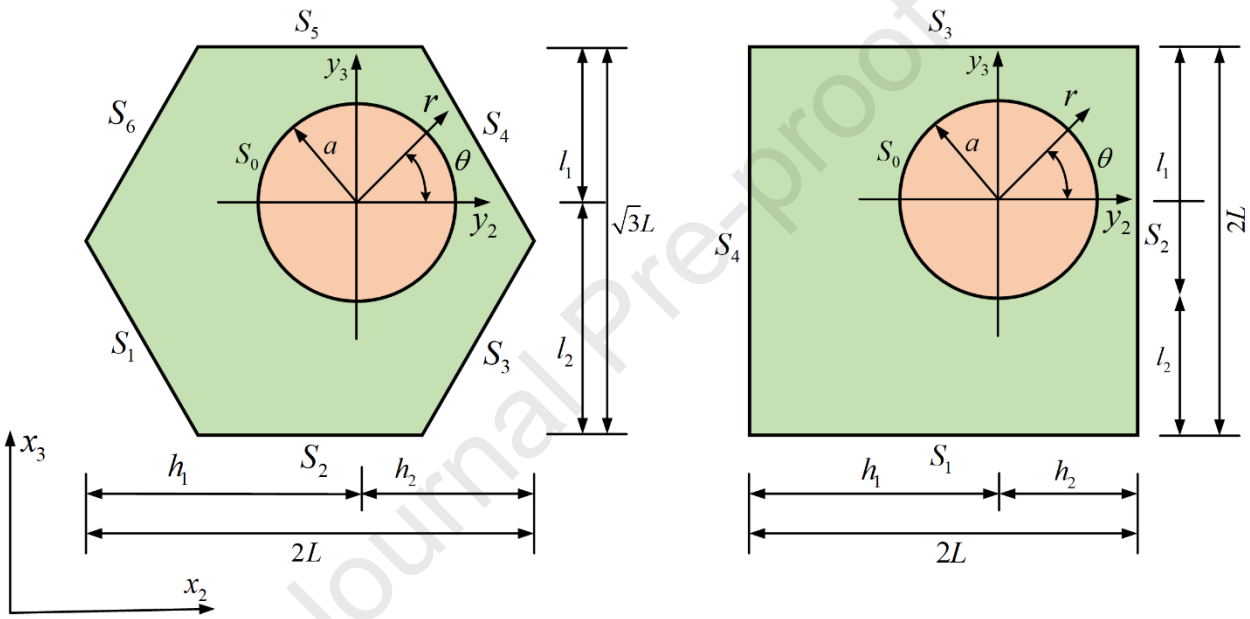

Figure 1 Hexagonal and square arrays of cylindrical fibers

$$\mathbf{u}^{(q)}\left(\mathbf{x},\mathbf{y}\right)=\bar{\boldsymbol{\varepsilon}}\cdot\mathbf{x}+\mathbf{u}'^{(q)}\left(\mathbf{y}\right) \tag{1}$$

In the above equation, $q=f,m$ indicates the fiber and matrix, respectively. $\mathbf{x}=\left(x_1,x_2,x_3\right)$ denotes the global coordinates and $\mathbf{y}=\left(y_1,y_2,y_3\right)$ represents the local coordinates with the origin positioned at the fiber center. The unit cell is loaded by the homogenized strain tensor $\bar{\boldsymbol{\varepsilon}}$. The $\mathbf{u}'^{(q)}\left(\mathbf{y}\right)$ indicates fluctuating displacement field induced by the microstructures and the

macroscopic strain. The above displacement field yields the local strain distributions in the two-scale form:

$$\boldsymbol{\varepsilon}^{(q)} = \overline{\boldsymbol{\varepsilon}} + \boldsymbol{\varepsilon}'^{(q)} = \overline{\boldsymbol{\varepsilon}} + \frac{1}{2}\left(\nabla \mathbf{u}'^{(q)} + \nabla \mathbf{u}'^{\mathrm{T}(q)}\right) \tag{2}$$

The constitutive equation for the fiber and matrix phases under infinitesimal deformations and rotations can be written as:

$$\boldsymbol{\sigma}^{(q)} = \mathbf{C}^{(q)} \cdot \boldsymbol{\varepsilon}^{(q)} = \mathbf{C}^{(q)} \cdot \overline{\boldsymbol{\varepsilon}} + \mathbf{C}^{(q)} \cdot \boldsymbol{\varepsilon}'^{(q)} \tag{3}$$

where $\boldsymbol{\sigma}^{(q)} = \left[\sigma_{11}, \sigma_{22}, \sigma_{33}, \sigma_{23}, \sigma_{13}, \sigma_{12}\right]^{(q)\mathrm{T}}$ denote stresses, $\boldsymbol{\varepsilon}^{(q)} = \left[\varepsilon_{11}, \varepsilon_{22}, \varepsilon_{33}, 2\varepsilon_{23}, 2\varepsilon_{13}, 2\varepsilon_{12}\right]^{(q)\mathrm{T}}$ denote strains, and $\mathbf{u}'^{(q)} = \left[u_1', u_2', u_3'\right]^{(q)\mathrm{T}}$ denotes displacements. ∇ indicates the gradient operator. $\mathbf{C}^{(q)}$ represents the fourth-order elastic stiffness tensor. The superscripts $q = f, m$ denote the fiber and matrix, respectively. In the case of a transversely isotropic bulk phase and the axis of symmetry aligned to the x_1 axis, the elastic stiffness tensor can be represented by:

$$\mathbf{C}^{(q)} = \begin{bmatrix} E_A + 4k_T\nu_A^2 & 2k_T\nu_A & 2k_T\nu_A & 0 & 0 & 0 \\ 2k_T\nu_A & k_T + \mu_T & k_T - \mu_T & 0 & 0 & 0 \\ 2k_T\nu_A & k_T - \mu_T & k_T + \mu_T & 0 & 0 & 0 \\ 0 & 0 & 0 & \mu_T & 0 & 0 \\ 0 & 0 & 0 & 0 & \mu_A & 0 \\ 0 & 0 & 0 & 0 & 0 & \mu_A \end{bmatrix}^{(q)} \tag{4}$$

where E_A, k_T, μ_T, μ_A and ν_A are the axial Young's modulus, transverse plane strain bulk modulus, transverse shear and axial shear moduli, and axial Poisson's ratio, respectively.

Before passing to the actual boundary value problem, it is crucial to represent all the fields and constitutive law, namely, in Cartesian coordinates with their cylindrical coordinate

counterparts. The axes in the Cartesian coordinates $\left(y_1, y_2, y_3\right)$ and the cylindrical coordinates $\left(z, r, \theta\right)$ are related via the following equations:

$$y_1 = z, \quad y_2 = r\cos\theta, \quad y_3 = r\sin\theta \tag{5}$$

Accordingly, the stress and strain vectors in Voigt notation are transformed between the cylindrical (indicated by the tilde symbol) and Cartesian coordinate systems as:

$$\begin{aligned} &\tilde{\mathbf{u}}' = \mathbf{R}\cdot\mathbf{u}', \qquad \tilde{\boldsymbol{\varepsilon}} = \mathbf{Q}_{\varepsilon}\cdot\boldsymbol{\varepsilon}, \qquad \tilde{\boldsymbol{\sigma}} = \mathbf{Q}_{\sigma}\cdot\boldsymbol{\sigma}, \\ &\mathbf{u}' = \mathbf{R}^{\mathrm{T}}\cdot\tilde{\mathbf{u}}', \qquad \boldsymbol{\varepsilon} = \mathbf{Q}_{\sigma}^{\mathrm{T}}\cdot\tilde{\boldsymbol{\varepsilon}}, \qquad \boldsymbol{\sigma} = \mathbf{Q}_{\varepsilon}^{\mathrm{T}}\cdot\tilde{\boldsymbol{\sigma}} \end{aligned} \tag{6}$$

where $\tilde{\mathbf{u}}' = \left[u_z', u_r', u_\theta'\right]^{(q)\mathrm{T}}$, $\tilde{\boldsymbol{\sigma}} = \left[\sigma_{zz}, \sigma_{rr}, \sigma_{\theta\theta}, \sigma_{r\theta}, \sigma_{zr}, \sigma_{z\theta}\right]^{\mathrm{T}}$, $\boldsymbol{\varepsilon} = \left[\varepsilon_{zz}, \varepsilon_{rr}, \varepsilon_{\theta\theta}, 2\varepsilon_{r\theta}, 2\varepsilon_{zr}, 2\varepsilon_{z\theta}\right]^{\mathrm{T}}$. $\mathbf{R}$ denotes the second-order rotator:

$$\mathbf{R} = \begin{bmatrix} 1 & 0 & 0 \\ 0 & \cos\theta & \sin\theta \\ 0 & -\sin\theta & \cos\theta \end{bmatrix} \tag{7}$$

$\mathbf{Q}_{\varepsilon}$ and $\mathbf{Q}_{\sigma}$ denote proper fourth-order rotators (Chatzigeorgiou et al., 2018; Chen et al., 2022):

$$\mathbf{Q}_{\varepsilon} = \begin{bmatrix} 1 & 0 & 0 & 0 & 0 & 0 \\ 0 & \cos^2\theta & \sin^2\theta & \frac{1}{2}\sin 2\theta & 0 & 0 \\ 0 & \sin^2\theta & \cos^2\theta & -\frac{1}{2}\sin 2\theta & 0 & 0 \\ 0 & -\sin 2\theta & \sin 2\theta & \cos 2\theta & 0 & 0 \\ 0 & 0 & 0 & 0 & \cos\theta & -\sin\theta \\ 0 & 0 & 0 & 0 & \sin\theta & \cos\theta \end{bmatrix} \tag{8}$$

$$\mathbf{Q}_\sigma = \begin{bmatrix} 1 & 0 & 0 & 0 & 0 & 0 \\ 0 & \cos^2\theta & \sin^2\theta & \sin 2\theta & 0 & 0 \\ 0 & \sin^2\theta & \cos^2\theta & -\sin 2\theta & 0 & 0 \\ 0 & -\frac{1}{2}\sin 2\theta & \frac{1}{2}\sin 2\theta & \cos 2\theta & 0 & 0 \\ 0 & 0 & 0 & 0 & \cos\theta & -\sin\theta \\ 0 & 0 & 0 & 0 & \sin\theta & \cos\theta \end{bmatrix} \tag{9}$$

In the theory of elasticity, the stress tensors $\boldsymbol{\sigma}^{(q)}$ in the fiber and matrix obey the following equilibrium equations:

$$\nabla \cdot \boldsymbol{\sigma}^{(q)} = \mathbf{0} \tag{10}$$

where $\nabla\cdot$ denotes the divergence operator. The use of generalized Hooke's law and the strain displacement relations:

$$\begin{aligned}
\varepsilon_{zz}^{(q)} &= \overline{\varepsilon}_{zz} + \frac{\partial u_z'^{(q)}}{\partial z} = \overline{\varepsilon}_{zz} \\
\varepsilon_{rr}^{(q)} &= \overline{\varepsilon}_{rr} + \frac{\partial u_r'^{(q)}}{\partial r} = \overline{\varepsilon}_{rr} + \varepsilon_{rr}'^{(q)} \\
\varepsilon_{\theta\theta}^{(q)} &= \overline{\varepsilon}_{\theta\theta} + \frac{u_r'^{(q)}}{r} + \frac{1}{r}\frac{\partial u_\theta'^{(q)}}{\partial \theta} = \overline{\varepsilon}_{\theta\theta} + \varepsilon_{\theta\theta}'^{(q)} \\
\varepsilon_{r\theta}^{(q)} &= \overline{\varepsilon}_{r\theta} + \frac{1}{2}\left(\frac{1}{r}\frac{\partial u_r'^{(q)}}{\partial \theta} + \frac{\partial u_\theta'^{(q)}}{\partial r} - \frac{u_\theta'^{(q)}}{r}\right) = \overline{\varepsilon}_{r\theta} + \varepsilon_{r\theta}'^{(q)} \\
\varepsilon_{rz}^{(q)} &= \overline{\varepsilon}_{rz} + \frac{1}{2}\frac{\partial u_z'^{(q)}}{\partial r} = \overline{\varepsilon}_{rz} + \varepsilon_{rz}'^{(q)} \\
\varepsilon_{\theta z}^{(q)} &= \overline{\varepsilon}_{\theta z} + \frac{1}{2r}\frac{\partial u_z'^{(q)}}{\partial \theta} = \overline{\varepsilon}_{\theta z} + \varepsilon_{\theta z}'^{(q)}
\end{aligned} \tag{11}$$

in the equilibrium equations in the cylindrical coordinates produces the Navier's displacement equations for the three unknown fluctuating displacements in each phase:

$$\begin{aligned}
&\frac{\partial^2 u_z'}{\partial r^2}+\frac{1}{r}\frac{\partial u_z'}{\partial r}+\frac{1}{r^2}\frac{\partial^2 u_z'}{\partial \theta^2}=0\\
&\left(k_T+\mu_T\right)\left(\frac{\partial^2 u_r'}{\partial r^2}+\frac{1}{r}\frac{\partial u_r'}{\partial r}-\frac{u_r'}{r^2}\right)+\frac{\mu_T}{r^2}\frac{\partial^2 u_r'}{\partial \theta^2}+\frac{k_T}{r}\frac{\partial^2 u_\theta'}{\partial r\partial \theta}-\frac{\left(k_T+2\mu_T\right)}{r^2}\frac{\partial u_\theta'}{\partial \theta}=0\\
&\mu_T\left(\frac{\partial^2 u_\theta'}{\partial r^2}+\frac{1}{r}\frac{\partial u_\theta'}{\partial r}-\frac{\tilde{u}_\theta}{r^2}\right)+\frac{\left(k_T+\mu_T\right)}{r^2}\frac{\partial^2 u_\theta'}{\partial \theta^2}+\frac{k_T}{r}\frac{\partial^2 u_r'}{\partial r\partial \theta}+\frac{\left(k_T+2\mu_T\right)}{r^2}\frac{\partial u_r'}{\partial \theta}=0
\end{aligned} \tag{12}$$

The solution for the unknown fluctuating displacements $u_z'^{(q)}\left(r,\theta\right)$, $u_r'^{(q)}\left(r,\theta\right)$ and $u_\theta'^{(q)}\left(r,\theta\right)$ is obtained subject to the periodicity boundary conditions of displacements and tractions, along with the continuity conditions at the fiber/matrix interface described in the sequel. It should be noted that the out-of-plane displacement $u_z'^{(q)}\left(r,\theta\right)$ and in-plane displacements $u_r'^{(q)}\left(r,\theta\right)$ and $u_\theta'^{(q)}\left(r,\theta\right)$ are uncoupled in the differential equations. Hence, they are solved independently for the displacement fields associated with respective loading as described in the following sections.

2.2 Axial normal and transverse loading

Under axial normal and transverse normal and shear loading, the fully coupled fluctuating displacements $u_r'^{(q)}\left(r,\theta\right)$ and $u_\theta'^{(q)}\left(r,\theta\right)$ for the fiber $\left(q=f\right)$ and matrix $\left(q=m\right)$ phases that fulfill the in-plane Navier's displacement equations take the form (Wang and Pindera, 2016):

$$\begin{aligned}
u_r'^{(q)}\left(r,\theta\right)&=F_{01}^{(q)}a\zeta+F_{02}^{(q)}a\zeta^{-1}+\sum_{n=2}^{\infty}\sum_{j=1}^{4}a\zeta^{p_{nj}}\left[F_{nj}^{(q)}\cos n\theta+G_{nj}^{(q)}\sin n\theta\right]\\
u_\theta'^{(q)}\left(r,\theta\right)&=\sum_{n=2}^{\infty}\sum_{j=1}^{4}a\beta_{nj}^{(q)}\zeta^{p_{nj}}\left[F_{nj}^{(q)}\sin n\theta-G_{nj}^{(q)}\cos n\theta\right]
\end{aligned} \tag{13}$$

where $\zeta=r/a$ denotes the normalized radial coordinate with regard to the fiber radius a. $p_{n1}=n+1,\quad p_{n2}=n-1,\quad p_{n3}=-(n+1),\quad p_{n4}=-(n-1)$ denote the four eigenvalues, and

$$\beta_{nj}^{(q)}=\frac{\left(k_T^{(q)}+\mu_T^{(q)}\right)\left(1-p_{nj}^2\right)+\mu_T^{(q)}n^2}{n\left(k_T^{(q)}p_{nj}-k_T^{(q)}-2\mu_T^{(q)}\right)} \tag{14}$$

In the above equations, $F_{nj}^{(q)}$ and $G_{nj}^{(q)}$ $\left(j=1,2,3,4\right)$ indicate unknown coefficients. It should be noted that $F_{02}^{(f)}=0$, $F_{n3}^{(f)}=F_{n4}^{(f)}=0$, and $G_{n3}^{(f)}=G_{n4}^{(f)}=0$ such that the fiber displacement remains bounded at $r=0$. Using the strain-displacement relation in Eq. (11), the fluctuating strain components in the cylindrical coordinates read:

$$\begin{aligned}
\varepsilon_{rr}'^{(q)}&=F_{01}^{(q)}-F_{02}^{(q)}\zeta^{-2}+\sum_{n=2}^{\infty}\sum_{j=1}^{4}p_{nj}\zeta^{p_{nj}-1}\left[F_{nj}^{(q)}\cos n\theta+G_{nj}^{(q)}\sin n\theta\right],\\
\varepsilon_{\theta\theta}'^{(q)}&=F_{01}^{(q)}+F_{02}^{(q)}\zeta^{-2}+\sum_{n=2}^{\infty}\sum_{j=1}^{4}\left(1+n\beta_{nj}^{(q)}\right)\zeta^{p_{nj}-1}\left[F_{nj}^{(q)}\cos n\theta+G_{nj}^{(q)}\sin n\theta\right],\\
\varepsilon_{r\theta}'^{(q)}&=\frac{1}{2}\sum_{n=2}^{\infty}\sum_{j=1}^{4}\left[\left(p_{nj}-1\right)\beta_{nj}^{(q)}-n\right]\zeta^{p_{nj}-1}\left(F_{nj}^{(q)}\sin n\theta-G_{nj}^{(q)}\cos n\theta\right)
\end{aligned} \tag{15}$$

The stress components in the cylindrical coordinates read:

$$\begin{aligned}
\sigma_{rr}^{(q)}&=2k_T^{(q)}\nu_A^{(q)}\overline{\varepsilon}_{11}+\left(k_T+\mu_T\right)^{(q)}\overline{\varepsilon}_{rr}+\left(k_T-\mu_T\right)^{(q)}\overline{\varepsilon}_{\theta\theta}\\
&+2k_T^{(q)}F_{01}-2\mu_T^{(q)}F_{02}^{(q)}\zeta^{-2}+\sum_{n=2}^{\infty}\sum_{j=1}^{4}P_{nj}^{(q)}\zeta^{p_{nj}-1}\left(F_{nj}^{(q)}\cos n\theta+G_{nj}^{(q)}\sin n\theta\right)\\
\sigma_{\theta\theta}^{(q)}&=2k_T^{(q)}\nu_A^{(q)}\overline{\varepsilon}_{11}+\left(k_T-\mu_T\right)^{(q)}\overline{\varepsilon}_{rr}+\left(k_T+\mu_T\right)^{(q)}\overline{\varepsilon}_{\theta\theta}\\
&+2k_T^{(q)}F_{01}^{(q)}+2\mu_T^{(q)}F_{02}^{(q)}\zeta^{-2}+\sum_{n=2}^{\infty}\sum_{j=1}^{4}Q_{nj}^{(q)}\zeta^{p_{nj}-1}\left(F_{nj}^{(q)}\cos n\theta+G_{nj}^{(q)}\sin n\theta\right)\\
\sigma_{r\theta}^{(q)}&=2\mu_T^{(q)}\overline{\varepsilon}_{r\theta}+\sum_{n=2}^{\infty}\sum_{j=1}^{4}R_{nj}^{(q)}\zeta^{p_{nj}-1}\left(F_{nj}^{(q)}\sin n\theta-G_{nj}^{(q)}\cos n\theta\right)
\end{aligned} \tag{16}$$

where $R_{nj}^{(q)}=\mu_T^{(q)}\left[\left(p_{nj}-1\right)\beta_{nj}^{(q)}-n\right]$, $P_{nj}^{(q)}=\left(k_T+\mu_T\right)^{(q)}p_{nj}+\left(k_T-\mu_T\right)^{(q)}\left(1+n\beta_{nj}^{(q)}\right)$, $Q_{nj}^{(q)}=\left(k_T-\mu_T\right)^{(q)}p_{nj}+\left(k_T+\mu_T\right)^{(q)}\left(1+n\beta_{nj}^{(q)}\right)$.

It should be noted that while the stresses and strains in Eqs. (15) and (16) can be evaluated analytically once the Fourier series parameters are obtained, the present work seeks to exploit the

automatic differentiation to compute effortlessly displacement partial derivatives with the Pytorch library. This greatly simplifies the construction of the network loss function and post-processing, with minimal human input. In this manuscript, we focus on a single circular fiber in a hexagonal or square unit cell. For multi-inclusion cases, the interactions between different inclusions introduce additional complexity. The current displacement functions in the matrix phase may require significant modifications and cannot be directly applied to such scenarios.

2.3 Axial shear loading

Under axial shear loading, the displacement field $u_z'^{(q)}(r,\theta)$ (or $u_1'^{(q)}(r,\theta)$) for the fiber and matrix phase that satisfies the out-of-plane Navier's displacement equations can be expressed as (Wang and Pindera, 2016):

$$u_z'^{(q)}(r,\theta) = H_{01}^{(q)} + \sum_{n=1}^{\infty} a\left[\left(\zeta^n H_{n1}^{(q)} + \zeta^{-n} H_{n3}^{(q)}\right)\cos n\theta + \left(\zeta^n H_{n2}^{(q)} + \zeta^{-n} H_{n4}^{(q)}\right)\sin n\theta\right] \tag{17}$$

where $H_{nj}^{(q)}$ $(j=1,2,3,4)$ are the unknown coefficients. $H_{n3}^{(q)} = H_{n4}^{(q)} = 0$ to ensure that the axial displacement $u_z'^{(q)}(r,\theta)$ is a finite value at $r=0$. Subsequently, the axial shear strain components in the cylindrical coordinates are obtained as:

$$\begin{aligned}
\varepsilon_{zr}'^{(q)} &= \frac{1}{2}\sum_{n=1}^{\infty} n\left[\left(\zeta^{n-1} H_{n1}^{(q)} - \zeta^{-n-1} H_{n3}^{(q)}\right)\cos n\theta + \left(\zeta^{n-1} H_{n2}^{(q)} - \zeta^{-n-1} H_{n4}^{(q)}\right)\sin n\theta\right] \\
\varepsilon_{z\theta}'^{(q)} &= \frac{1}{2}\sum_{n=1}^{\infty} n\left[-\left(\zeta^{n-1} H_{n1}^{(q)} + \zeta^{-n-1} H_{n3}^{(q)}\right)\sin n\theta + \left(\zeta^{n-1} H_{n2}^{(q)} + \zeta^{-n-1} H_{n4}^{(q)}\right)\cos n\theta\right]
\end{aligned} \tag{18}$$

The stress components in the cylindrical coordinates read:

$$\begin{aligned}
\sigma_{zr}^{(q)} &= 2\mu_A^{(q)}\bar{\varepsilon}_{zr} + \mu_A^{(q)}\sum_{n=1}^{\infty} n\left[\left(\zeta^{n-1} H_{n1}^{(q)} - \zeta^{-n-1} H_{n3}^{(q)}\right)\cos n\theta + \left(\zeta^{n-1} H_{n2}^{(q)} - \zeta^{-n-1} H_{n4}^{(q)}\right)\sin n\theta\right] \\
\sigma_{z\theta}^{(q)} &= 2\mu_A^{(q)}\bar{\varepsilon}_{z\theta} + +\mu_A^{(q)}\sum_{n=1}^{\infty} n\left[-\left(\zeta^{n-1} H_{n1}^{(q)} + \zeta^{-n-1} H_{n3}^{(q)}\right)\sin n\theta + \left(\zeta^{n-1} H_{n3}^{(q)} + \zeta^{-n-1} H_{n4}^{(q)}\right)\cos n\theta\right]
\end{aligned} \tag{19}$$

3. Fourier homogenization network

In this section, the machine learning technique is harnessed to represent the fluctuating displacements in the fiber and matrix phases that satisfy the periodicity boundary conditions and the continuity conditions at the fiber/matrix interface. We aim to establish the following mapping functions:

$$\left[u_r', u_\theta'\right]^{(f)} = FHN_{in}^{(f)}\left[r,\theta\right], \quad \left[u_r', u_\theta'\right]^{(m)} = FHN_{in}^{(m)}\left[r,\theta\right] \tag{20}$$

namely, a mapping from $\mathbb{R}^2 \to \mathbb{R}^2$. The in-plane fluctuating displacement fields $\left[u_r', u_\theta'\right]^{(q)}$ under in-plane loading by $\boldsymbol{\varepsilon}^{in} = \left[\overline{\varepsilon}_{11}, \overline{\varepsilon}_{22}, \overline{\varepsilon}_{33}, 2\overline{\varepsilon}_{23}\right]^{\mathrm{T}}$ are obtained by minimizing the following loss function:

$$\text{ArgMin}: \mathcal{L}\left(u_r', u_\theta'\right) = \mathcal{L}_{S_0} + \mathcal{L}_b \tag{21}$$

where

$$\begin{aligned}\mathcal{L}_{S_0} = &\frac{1}{N_0}\sum_{k=1}^{k=N_0}\gamma_{0k}^{\sigma}\left[\left(\frac{\sigma_{rr}^{(f)}\left(S_{0k}\right)-\sigma_{rr}^{(m)}\left(S_{0k}\right)}{k_T^{(m)}+\mu_T^{(m)}}\right)+\left(\frac{\sigma_{r\theta}^{(f)}\left(S_{0k}\right)-\sigma_{r\theta}^{(m)}\left(S_{0k}\right)}{2\mu_T^{(m)}}\right)^2\right] \\ &+\frac{1}{N_0}\sum_{k=1}^{k=N_0}\gamma_{0k}^{u}\left[\left(u_r'^{(f)}\left(S_{0k}\right)-u_r'^{(m)}\left(S_{0k}\right)\right)^2+\left(u_\theta'^{(f)}\left(S_{0k}\right)-u_\theta'^{(m)}\left(S_{0k}\right)\right)^2\right]\end{aligned} \tag{22}$$

for the hexagonal arrays $\mathcal{L}_b = \mathcal{L}_{S_1-S_4} + \mathcal{L}_{S_2-S_5} + \mathcal{L}_{S_3-S_6}$ with:

$$\begin{aligned}\mathcal{L}_{S_1-S_4} = &\frac{1}{N_1}\sum_{k=1}^{k=N_1}\gamma_{1k}^{\sigma}\left[\left(\frac{t_2^{(m)}\left(S_{1k}\right)-t_2^{(m)}\left(S_{4k}\right)}{k_T^{(m)}+\mu_T^{(m)}}\right)+\left(\frac{t_3^{(m)}\left(S_{1k}\right)-t_3^{(m)}\left(S_{4k}\right)}{\mu_T^{(m)}}\right)^2\right] \\ &+\frac{1}{N_1}\sum_{k=1}^{k=N_1}\gamma_{1k}^{u}\left[\left(u_2'^{(m)}\left(S_{1k}\right)-u_2'^{(m)}\left(S_{4k}\right)\right)^2+\left(u_3'^{(m)}\left(S_{1k}\right)-u_3'^{(m)}\left(S_{4k}\right)\right)^2\right]\end{aligned} \tag{23}$$

$$\mathcal{L}_{S_2-S_5}=\frac{1}{N_2}\sum_{k=1}^{k=N_2}\gamma_{2k}^{\sigma}\left[\left(\frac{t_2^{(m)}\left(S_{2k}\right)-t_2^{(m)}\left(S_{5k}\right)}{k_T^{(m)}+\mu_T^{(m)}}\right)+\left(\frac{t_3^{(m)}\left(S_{2k}\right)-t_3^{(m)}\left(S_{5k}\right)}{\mu_T^{(m)}}\right)^2\right]$$
$$+\frac{1}{N_2}\sum_{k=1}^{k=N_2}\gamma_{2k}^{u}\left[\left(u_2'^{(m)}\left(S_{2k}\right)-u_2'^{(m)}\left(S_{5k}\right)\right)^2+\left(u_3'^{(m)}\left(S_{2k}\right)-u_3'^{(m)}\left(S_{5k}\right)\right)^2\right] \tag{24}$$

$$\mathcal{L}_{S_3-S_6}=\frac{1}{N_3}\sum_{k=1}^{k=N_3}\gamma_{3k}^{\sigma}\left[\left(\frac{t_2^{(m)}\left(S_{3k}\right)-t_2^{(m)}\left(S_{6k}\right)}{k_T^{(m)}+\mu_T^{(m)}}\right)+\left(\frac{t_3^{(m)}\left(S_{3k}\right)-t_3^{(m)}\left(S_{6k}\right)}{\mu_T^{(m)}}\right)^2\right]$$
$$+\frac{1}{N_3}\sum_{k=1}^{k=N_3}\gamma_{3k}^{u}\left[\left(u_2'^{(m)}\left(S_{3k}\right)-u_2'^{(m)}\left(S_{6k}\right)\right)^2+\left(u_3'^{(m)}\left(S_{3k}\right)-u_3'^{(m)}\left(S_{6k}\right)\right)^2\right] \tag{25}$$

for square arrays $\mathcal{L}_b=\mathcal{L}_{S_1-S_3}+\mathcal{L}_{S_2-S_4}$ with:

$$\mathcal{L}_{S_1-S_3}=\frac{1}{N_1}\sum_{k=1}^{k=N_1}\gamma_{1k}^{\sigma}\left[\left(\frac{t_2^{(m)}\left(S_{1k}\right)-t_2^{(m)}\left(S_{3k}\right)}{k_T^{(m)}+\mu_T^{(m)}}\right)+\left(\frac{t_3^{(m)}\left(S_{1k}\right)-t_3^{(m)}\left(S_{3k}\right)}{\mu_T^{(m)}}\right)^2\right]$$
$$+\frac{1}{N_1}\sum_{k=1}^{k=N_1}\gamma_{1k}^{u}\left[\left(u_2'^{(m)}\left(S_{1k}\right)-u_2'^{(m)}\left(S_{3k}\right)\right)^2+\left(u_3'^{(m)}\left(S_{1k}\right)-u_3'^{(m)}\left(S_{3k}\right)\right)^2\right] \tag{26}$$

$$\mathcal{L}_{S_2-S_4}=\frac{1}{N_2}\sum_{k=1}^{k=N_2}\gamma_{2k}^{\sigma}\left[\left(\frac{t_2^{(m)}\left(S_{2k}\right)-t_2^{(m)}\left(S_{4k}\right)}{k_T^{(m)}+\mu_T^{(m)}}\right)+\left(\frac{t_3^{(m)}\left(S_{2k}\right)-t_3^{(m)}\left(S_{4k}\right)}{\mu_T^{(m)}}\right)^2\right]$$
$$+\frac{1}{N_2}\sum_{k=1}^{k=N_2}\gamma_{2k}^{u}\left[\left(u_2'^{(m)}\left(S_{2k}\right)-u_2'^{(m)}\left(S_{4k}\right)\right)^2+\left(u_3'^{(m)}\left(S_{2k}\right)-u_3'^{(m)}\left(S_{4k}\right)\right)^2\right] \tag{27}$$

In the above equations, S_{ik} denotes the kth collocation points on the S_i face. N_0 and N_i denotes the total number of collocation points on the fiber/matrix interface S_0 and the S_i face, respectively. $t_i=\sigma_{ij}n_j$ denotes the traction components from Cauchy's relation. γ_{ik}^{σ} and γ_{ik}^{u} are trainable weights associated with kth collocation point on the ith face in each traction and displacement loss term, respectively.

Similarly, under out-of-plane loading by $\boldsymbol{\varepsilon}^{out}=\left[2\bar{\varepsilon}_{12},2\bar{\varepsilon}_{13}\right]^{\mathrm{T}}$, we have

$$\left[u_1'\right]^{(f)} = FHN_{out}^{(f)}\left[r,\theta\right], \quad \left[u_1'\right]^{(m)} = FHN_{out}^{(m)}\left[r,\theta\right] \tag{28}$$

namely, a mapping from $\mathbb{R}^2 \to \mathbb{R}^1$. The out-of-plane fluctuating displacement fields $\left[u_1'\right]^{(q)}$ are obtained by minimizing the following loss function:

$$\text{ArgMin}: \mathcal{L}\left(u_1'\right) = \mathcal{L}_{S_0} + \mathcal{L}_b \tag{29}$$

where

$$\mathcal{L}_{S_0} = \frac{1}{N_0}\sum_{k=1}^{k=N_0}\left[\gamma_{0k}^{\sigma}\left(\frac{\sigma_{zr}^{(f)}\left(S_{0k}\right)-\sigma_{zr}^{(m)}\left(S_{0k}\right)}{\mu_T^{(m)}}\right)^2 + \gamma_{0k}^{u}\left(u_1'^{(f)}\left(S_{0k}\right)-u_1'^{(m)}\left(S_{0k}\right)\right)^2\right] \tag{30}$$

for the hexagonal arrays $\mathcal{L}_b = \mathcal{L}_{S_1-S_4} + \mathcal{L}_{S_2-S_5} + \mathcal{L}_{S_3-S_6}$ with:

$$\mathcal{L}_{S_1-S_4} = \frac{1}{N_1}\sum_{k=1}^{k=N_1}\left[\gamma_{1k}^{\sigma}\left(\frac{t_1^{(m)}\left(S_{1k}\right)-t_1^{(m)}\left(S_{4k}\right)}{\mu_T^{(m)}}\right)^2 + \gamma_{1k}^{u}\left(u_1'^{(m)}\left(S_{1k}\right)-u_1'^{(m)}\left(S_{4k}\right)\right)^2\right] \tag{31}$$

$$\mathcal{L}_{S_2-S_5} = \frac{1}{N_2}\sum_{k=1}^{k=N_2}\left[\gamma_{2k}^{\sigma}\left(\frac{t_1^{(m)}\left(S_{2k}\right)-t_1^{(m)}\left(S_{5k}\right)}{\mu_T^{(m)}}\right)^2 + \gamma_{2k}^{u}\left(u_1'^{(m)}\left(S_{2k}\right)-u_1'^{(m)}\left(S_{5k}\right)\right)^2\right] \tag{32}$$

$$\mathcal{L}_{S_3-S_6} = \frac{1}{N_3}\sum_{k=1}^{k=N_3}\left[\gamma_{3k}^{\sigma}\left(\frac{t_1^{(m)}\left(S_{3k}\right)-t_1^{(m)}\left(S_{6k}\right)}{\mu_T^{(m)}}\right)^2 + \gamma_{3k}^{u}\left(u_1'^{(m)}\left(S_{3k}\right)-u_1'^{(m)}\left(S_{6k}\right)\right)^2\right] \tag{33}$$

for square arrays $\mathcal{L}_b = \mathcal{L}_{S_1-S_3} + \mathcal{L}_{S_2-S_4}$ with:

$$\mathcal{L}_{S_1-S_4} = \frac{1}{N_1}\sum_{k=1}^{k=N_1}\left[\gamma_{1k}^{\sigma}\left(\frac{t_1^{(m)}\left(S_{1k}\right)-t_1^{(m)}\left(S_{3k}\right)}{\mu_T^{(m)}}\right)^2 + \gamma_{1k}^{u}\left(u_1'^{(m)}\left(S_{1k}\right)-u_1'^{(m)}\left(S_{3k}\right)\right)^2\right] \tag{34}$$

$$\mathcal{L}_{S_2-S_4} = \frac{1}{N_2}\sum_{k=1}^{k=N_2}\left[\gamma_{2k}^{\sigma}\left(\frac{t_1^{(m)}\left(S_{2k}\right)-t_1^{(m)}\left(S_{4k}\right)}{\mu_T^{(m)}}\right)^2 + \gamma_{2k}^{u}\left(u_1'^{(m)}\left(S_{2k}\right)-u_1'^{(m)}\left(S_{4k}\right)\right)^2\right] \tag{35}$$

In summary, the trainable parameters of the Fourier homogenization network include:

In-plane loading: $F_{01}^{(m)}$, $F_{02}^{(m)}$, $F_{n1}^{(m)}$, $G_{n1}^{(m)}$, $F_{n2}^{(m)}$, $G_{n2}^{(m)}$, $F_{n3}^{(m)}$, $G_{n3}^{(m)}$, $F_{n4}^{(m)}$, $G_{n4}^{(m)}$, $F_{01}^{(f)}$, $F_{n1}^{(f)}$, $F_{n2}^{(f)}$, $G_{n1}^{(m)}$, $G_{n2}^{(m)}$, γ_{ik}^{σ}, γ_{ik}^{u}

Out-of-plane loading: $H_{n1}^{(m)}$, $H_{n2}^{(m)}$, $H_{n3}^{(m)}$, $H_{n4}^{(m)}$ $H_{n1}^{(f)}$, $H_{n2}^{(f)}$, γ_{ik}^{σ}, γ_{ik}^{u}

During the training of the network model, we attempt to minimize the total loss function $\mathcal{L}\left(u_r', u_\theta'\right)$ or $\mathcal{L}\left(u_1'\right)$ with regard to the Fourier series parameters $\boldsymbol{\theta}$ based on the gradient descent, but concurrently maximize the total loss function about the adaptive weights $\boldsymbol{\gamma}$ based on the gradient ascent as follows (Chen et al., 2024; McClenny and Braga-Neto, 2023; Wu et al., 2024):

$$\begin{aligned} \boldsymbol{\theta}^{l+1} &= \boldsymbol{\theta}^{l} - \eta_l \nabla_{\boldsymbol{\theta}} \mathcal{L}\left(\boldsymbol{\theta}, \boldsymbol{\lambda}\right), \\ \boldsymbol{\lambda}^{l+1} &= \boldsymbol{\lambda}^{l} + \rho_l \nabla_{\boldsymbol{\lambda}} \mathcal{L}\left(\boldsymbol{\theta}, \boldsymbol{\lambda}\right) \end{aligned} \tag{36}$$

where l indicates the lth training epoch. η_l and ρ_l indicate the non-negative learning rates for the Fourier series parameters and adaptive weights $\boldsymbol{\gamma}$, respectively. Fourier series parameters under arbitrary strain components, and hence the fluctuating displacement fields, can be obtained when the total loss function is minimized. The strain field can be calculated by using the automatic differentiation in PyTorch library, verified using the analytical expressions.

4. Verifications

In this section, we examine the modelling and predictive capabilities of the Fourier homogenization network model by comparison against the benchmark results generated by the finite-element simulation of hexagonal and square arrays of cylindrical fiber with several volume fractions and loading scenarios. The material system employed in this manuscript is a

graphite/epoxy composite whose constituent phase moduli are listed in Table 1. While the AS4 graphite fiber is transversely isotropic, the epoxy matrix is isotropic.

Table 1 Elastic fiber and matrix properties employed in the calculations

Material	E_A(GPa)	E_T(GPa)	μ_A(GPa)	μ_T(GPa)	ν_A
AS4 graphite fiber	225	15	15	7	0.2
Epoxy	4.2	4.2	1.567	1.567	0.34

First of all, a hexagonal unit cell with 20% of fiber volume fraction was considered. A uniaxial transverse strain $\bar{\varepsilon}_{22} = 1\%$ was applied with all other strain components set to zeros. To investigate the effect of harmonic term numbers on the accuracy of the Fourier homogenization network, four network models with increasing number of harmonic terms were constructed, namely, $n = 2$, $n = 5$, $n = 8$ and $n = 12$. The network was trained with Adam Optimizer in PyTorch. The initial learning rate η_1 for unknown Fourier series coefficients was set to 0.01 and decreased by 50% for every 5k epoch. The initial learning rate ρ_1 for collocation point weights was set to the same value and decay rate but it remains constant after 15k epochs.

The number of residual points in the fiber/matrix interface is $N_0 = 360$ while the number of points at the unit cell six edges is $N_1 = N_2 = N_3 = 200$. These points are evenly distributed along their respective surfaces. The network performance as a function of training epochs is illustrated in Figure 2. It is observed that as the number of harmonic terms increases, there is a tendency for the predicted loss residuals to decrease, although accompanied by a noticeable rise in the fluctuation of loss values.

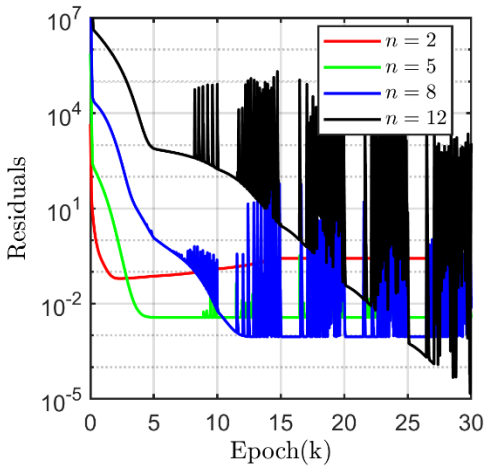

Figure 2 Loss values as a function of training epoch for four different numbers of harmonic terms

Figure 3 presents comparison of fluctuating displacement component u_2' distributions with the studied harmonic terms, taken from the checkpoint at 30k epochs. Figure 4 shows the difference in fluctuating displacement u_2' distribution between the Fourier homogenization network and the 8-noded finite-element reference results. As anticipated, the utilization of 2 harmonic terms is inadequate in capturing displacement field distributions. Conversely, when employing 5, 8, and 12 harmonic terms, the results for the fluctuating displacement distributions appear almost identical. As the number of harmonic terms increases, the network solution gradually converges towards the finite-element solution (see Figure 4). Notably, with the application of 12 harmonic terms, any distinctions between the network model and finite element prediction become imperceptible. Therefore, unless otherwise stated, 12 harmonic terms will be utilized in generating the results that follow.

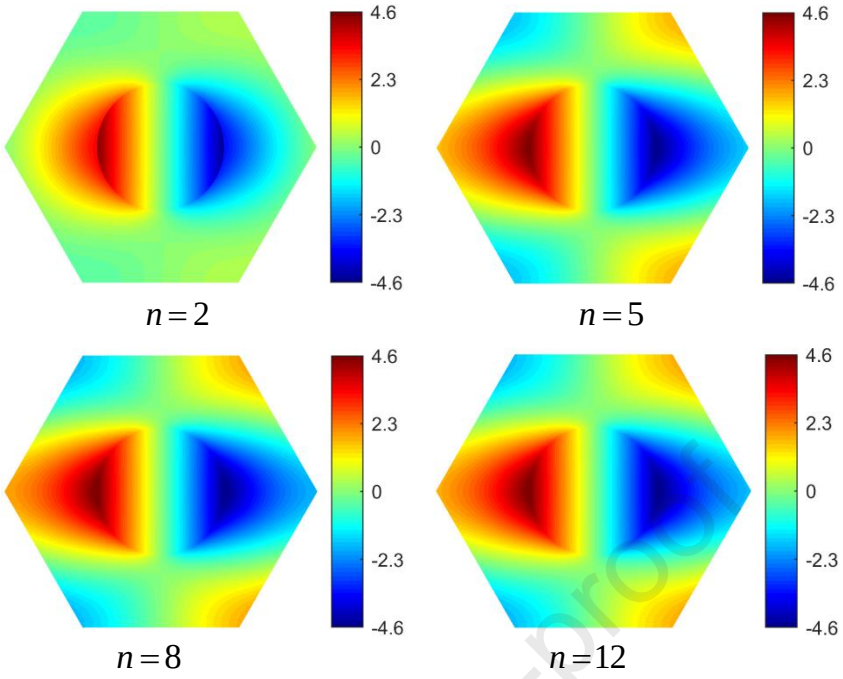

Figure 3 Comparison of fluctuating displacement $u_2'\left(10^{-3}\mu m\right)$ in a hexagonal unit cell as a function of the number of harmonics at the applied strain $\bar{\varepsilon}_{22}=1\%$

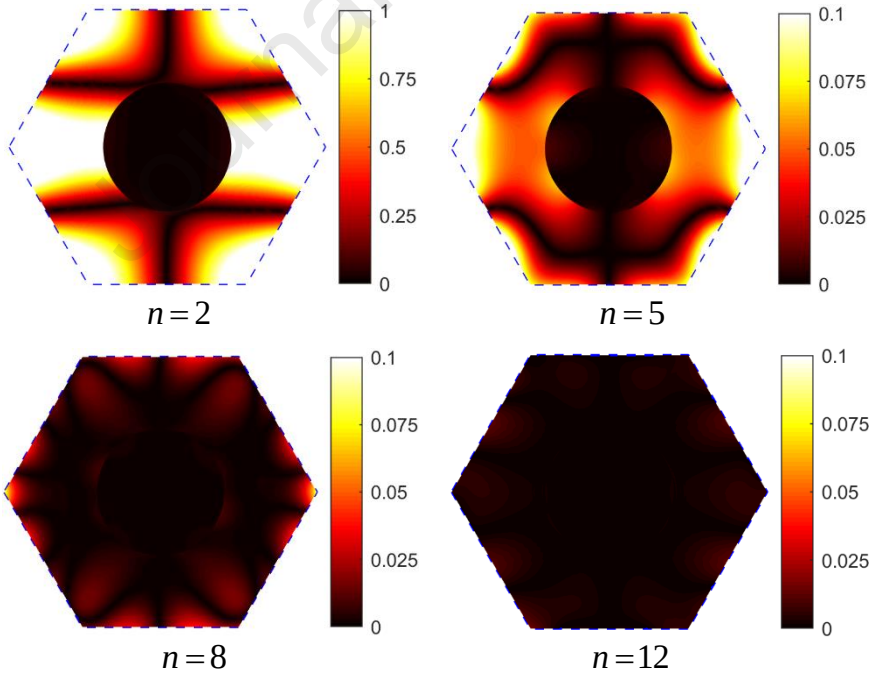

Figure 4 Comparison of difference in fluctuating displacement $u_2'\left(\times 1000\right)$ with respect to FEM predictions in a hexagonal unit cell as a function of the number of harmonics at the applied strain $\bar{\varepsilon}_{22}=1\%$

Comparison of the local stress field σ_{22}, σ_{33} and σ_{23} generated by the network and finite-element results for two specific harmonic terms $n=5$ and $n=12$ is presented in Figure 5. The absolute differences between the network and finite-element predictions are displayed in Figure 6. Once again, the network approach shows a high level of accordance with the finite-element results even with only 5 harmonic terms. When the harmonic terms increase to 12, the differences between the proposed method and the reference solution vanish.

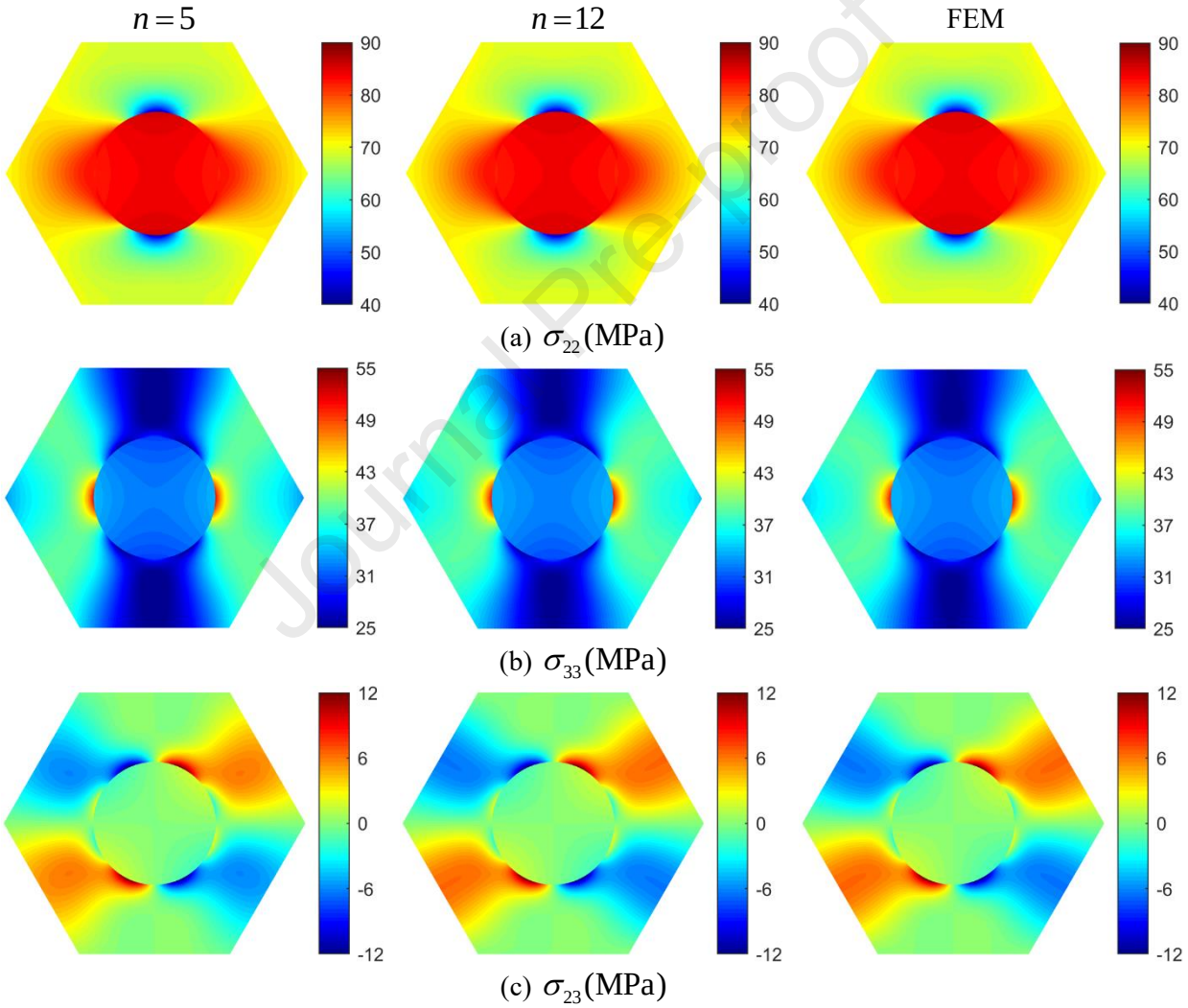

Figure 5 Comparison of local stress field predictions in a hexagonal unit cell with 5 and 12 harmonics and finite-element simulation at the applied strain $\bar{\varepsilon}_{22}=1\%$

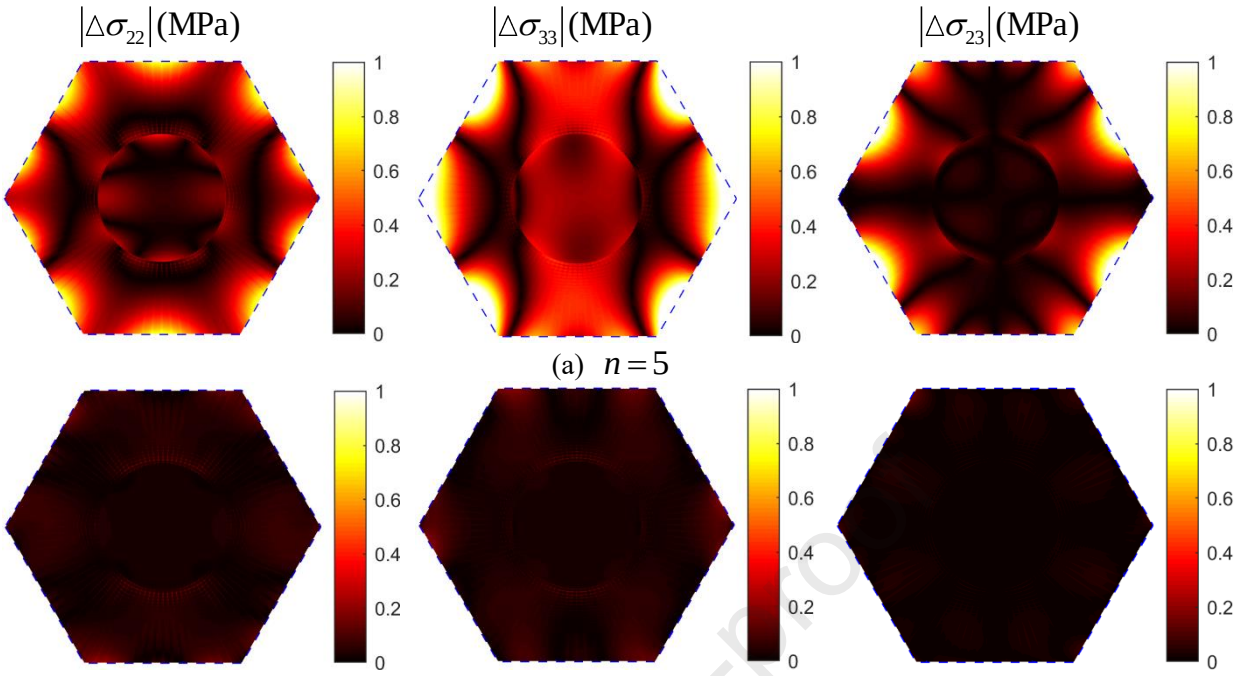

(a) $n=5$

(b) $n=12$

Figure 6 Comparison of difference in stress distributions with respect to FEM predictions in a hexagonal unit cell as a function of the number of harmonics at the applied strain $\bar{\varepsilon}_{22}=1\%$

As depicted in Figure 7, in order to demonstrate the fulfillment of the continuity condition at the fiber/matrix interface, we compare the interfacial radial and tangential stresses σ_{rr}, $\sigma_{r\theta}$ and fluctuating displacements u_r' and u_θ' as a function of angular position. Exceptional correlations are observed in the generated stresses and displacements on both the fiber and matrix sides of the interface, suggesting the continuity conditions are indeed satisfied by the network models.

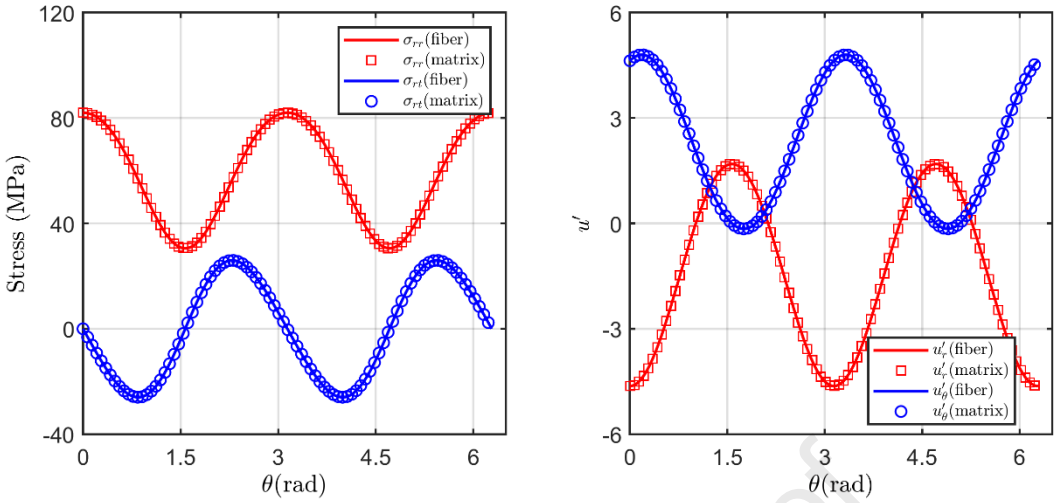

Figure 7 Comparison of the difference in interfacial normal and tangential stresses and displacements at the fiber and matrix sides in a hexagonal unit cell with 12 harmonics

Figure 8 shows comparison of the Fourier homogenization network's prediction of transverse shear stress distribution σ_{23} with finite-element results, subjected to transverse shear loading $\bar{\varepsilon}_{23} = 1\%$. Hexagonal and square arrays with a high fiber volume fraction (60%) were employed to highlight the important adjacent fiber interactions. This choice also serves to create a more challenging and thorough evaluation of the network's capability to accurately represent interfacial continuity and periodicity boundary conditions at high-volume fractions. Figure 8 suggests that both qualitative and quantitative characters of the stress field are well-captured by the network approach relative to the finite-element simulations. The absolute differences of the predicted transverse shear stresses by the two approaches are depicted in Figure 9. These differences are negligible relative to actual values of the stress magnitude.

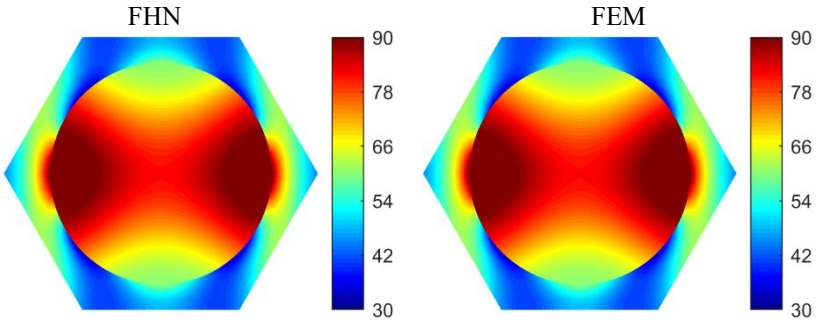

(a) Hexagonal array

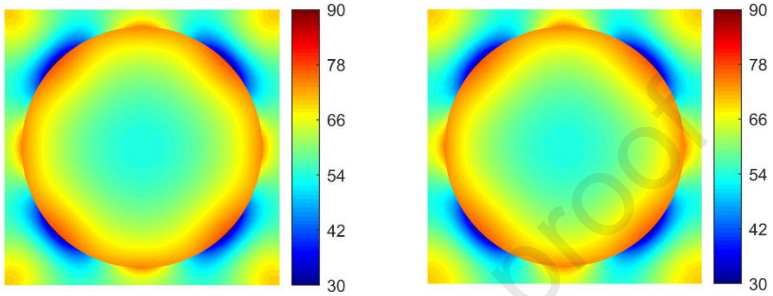

(b) Square array

Figure 8 Comparison of stress distribution $\sigma_{23}\left(\mathrm{MPa}\right)$ in a hexagonal unit cell with 60% fiber volume fraction in hexagonal and square unit cells at the applied strain $\bar{\varepsilon}_{23}=1\%$

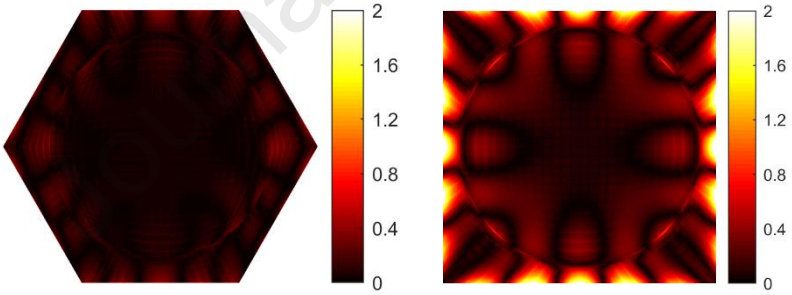

(a) Hexagonal array (b) Square array

Figure 9 Comparison of difference in stress distributions $\left|\triangle\sigma_{23}\right|\left(\mathrm{MPa}\right)$ with respect to FEM predictions in hexagonal and square unit cells at the applied strain $\bar{\varepsilon}_{23}=1\%$

The corresponding stress distributions σ_{12} and σ_{13} under the out-of-plane axial shear loading $\bar{\varepsilon}_{12}=1\%$ are presented in Figure 10. A hexagonal unit cell with 20% volume fraction was considered. The presence of an offset fiber within the unit cell introduces additional complexity, posing a challenge to ensuring the fulfillment of periodicity boundary conditions using the network

approach. This challenge arises from stress localization occurring near the edges of the unit cell. Once again, the proposed method correlates well with the finite-element predictions.

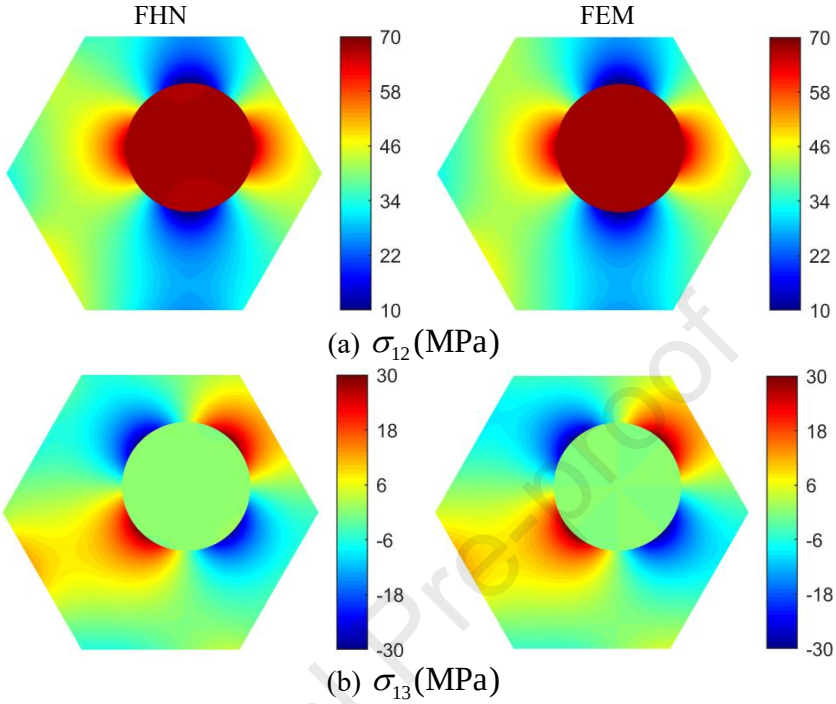

Figure 10 Comparison of axial shear stress distribution $\sigma_{12}\left(\mathrm{MPa}\right)$ and $\sigma_{13}\left(\mathrm{MPa}\right)$ in a hexagonal unit cell with offset fiber at the applied strain $\bar{\varepsilon}_{12}=1\%$

5. Transfer learning

In this section, we propose a transfer learning strategy to mitigate the computational challenges of the FHN approach. The core idea is to leverage the trained parameters of a pre-existing neural network for efficiently training models with new geometries. This is inspired by the observation that, under similar loading conditions, changes in the fiber volume fraction, or adjusting the fiber center position, the spatial distributions of stresses inside the unit cells are not fundamentally altered.

Herein, we consider a hexagonal unit cell with a 25% fiber volume fraction at the applied strain $\bar{\varepsilon}_{22}=1\%$. The fiber center is translated from the origin to the new position (0.2,0.2). Instead

of directly training a new FHN model from scratch, we first copy all the trained network parameters from the network in Figure 2. In the second step, during the re-training of the new geometries, these network parameters are fine-tuned. It should be emphasized that a smaller learning rate (namely, 0.001) was utilized in the transfer learning procedure to avoid significant updating of the parameters copied from the trained model. Figure 11 compares the transfer learning loss function with that from direct training of the neural network model. The results show that the transfer learning loss decreases rapidly, reaching a value below 10^{-3} after around 4k epochs. In contrast, direct training of the same FHN model from scratch results in a significantly higher loss value. Figure 12 shows the distributions of transverse normal stresses σ_{22} generated with the transfer learning FHN and the FEM results. The direct training results have not been shown due to significant discrepancies with the FEM benchmark solutions. As anticipated, the transfer learning FHN predicted stresses show a high level of accordance with those of FEM.

It is worth noting that, despite the demonstrated accuracy, the proposed FHN technique cannot compete with traditional approaches such as FEM in terms of computational efficiency since the FHN transforms a linear elasticity unit cell problem into a nonlinear optimization problem. To obtain the unit cell solutions for up to 30k epochs, as shown in Figure 5, the FHN training process consumes 3300 seconds, while the FEM takes only 27 seconds based on 2880 eight-node quadratic elements. These simulations are performed on a personal computer with 13th Gen Intel(R) Core (TM) I9-13900H @ 2.60 GHz, 32 GB memory, NVIDIA@ RTX TM4070 GPU, 24 GB memory, 64-bit operating system, and x64-based processor. Using the transfer learning technique, the solution for new geometries can be significantly sped up, which takes 1078s to retrain the neural network model for up to 10k epochs, offering a substantial acceleration compared to the direct training of the original model.

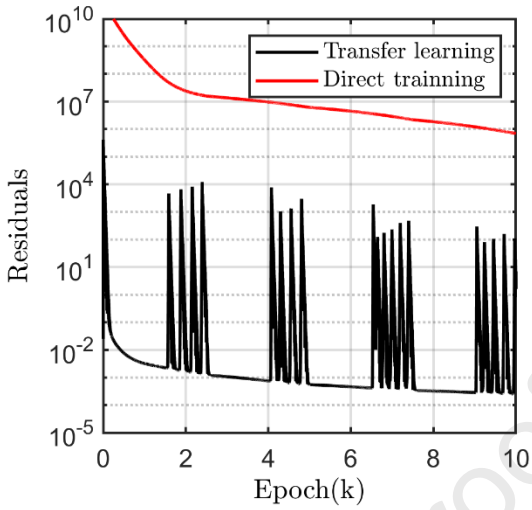

Figure 11 Comparison of loss functions between transfer learning and direct training of the neural network model

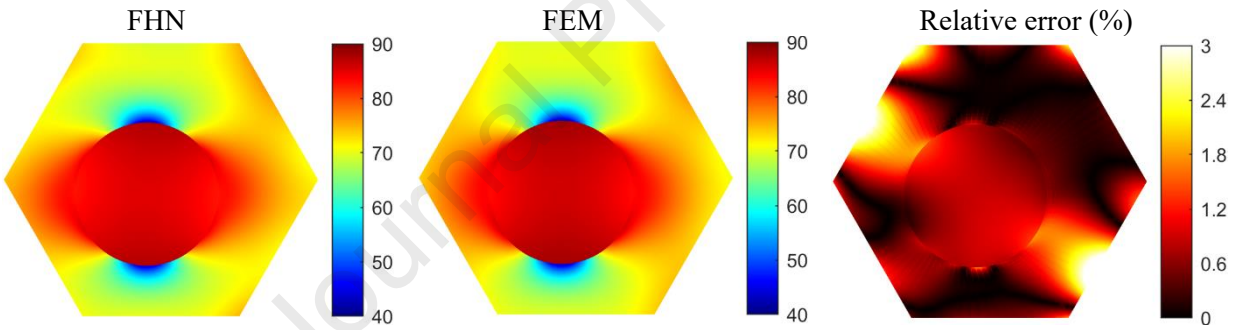

Figure 12 Comparison of transverse normal stress $\sigma_{22}\left(\mathrm{MPa}\right)$ distribution in a hexagonal unit cell with offset fiber at the applied strain $\bar{\varepsilon}_{22}=1\%$

6. Cohesive interfacial damage

The interface between the fiber and matrix plays an indispensable role in affecting the stress transfer mechanism and thus the failure behavior and the overall response of the composites. To naturally track the interfacial debonding, the interface can be modelled by the cohesive zone model (CZM) originally proposed by Barenblatt (1959) and Dugdale (1960). The contributions of Needleman and coworkers (Needleman, 1987; Xu and Needleman, 1994) and Ortiz and coworkers

(Camacho and Ortiz, 1996; Ortiz and Suresh, 1993) have significantly advanced the utilization of CZM in modeling fracture phenomena across various material systems. In the CZM model, the displacement discontinuity is admissible while the traction continuity condition is preserved for the interface undergoing separation, described by a traction separation relation. To further demonstrate the capabilities of the FHN method for modelling evolving interfacial damage in composites, we introduce the cohesive interface into the developed framework. Hereafter, we examine an exponential cohesive law as follows (see Figure 13):

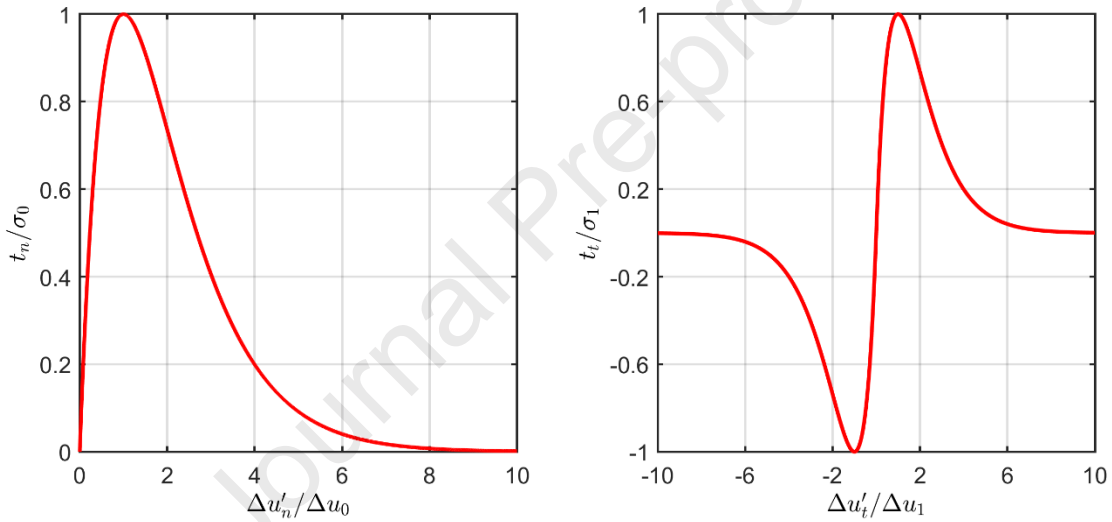

(a) Normal traction-normal separation (b) Tangential traction – tangential separation

Figure 13 Normal and tangential traction-separation relations

$$t_n = \sigma_0 \frac{\Delta u_n'}{\Delta u_0} \exp\left(1 - \frac{\Delta u_n'}{\Delta u_0}\right), \quad \Delta u_n' \geq 0 \tag{37}$$

$$t_t = \begin{cases} \sigma_1 \dfrac{\Delta u_t'}{\Delta u_1} \exp\left(1 - \dfrac{\Delta u_t'}{\Delta u_1}\right), & \Delta u_t' \geq 0 \\ \sigma_1 \dfrac{\Delta u_t'}{\Delta u_1} \exp\left(1 + \dfrac{\Delta u_t'}{\Delta u_1}\right), & \Delta u_t' < 0 \end{cases} \tag{38}$$

In the above equations, t_n and t_t are the normal and tangential tractions. $\Delta u_i' = u_i'^{(m)} - u_i'^{(f)}$. σ_0, σ_1, Δu_0 and Δu_1 denote interface failure (critical) stress and separation distance respectively for normal and shear directions. The majority of the CZM applications are based on the numerical approaches, in particular, the finite-element/finite-volume based methods. It is noted that when the interface is under compressive normal stress, the displacement discontinuity needs to be set to zero directly, $\Delta u_n = 0$, in order to avoid material interpenetration. To implement the cohesive interface model in the proposed approach, only the interface loss term needs to be modified while other loss terms remain intact:

for in-plane loading:

$$\begin{aligned}\mathcal{L}_{S_0} = \frac{1}{N_0}\sum_{k=1}^{k=N_0}\gamma_{0k}^{\sigma}\left[\left(\frac{\sigma_{rr}^{(f)}(S_{0k})-t_n(S_{0k})}{k_T^{(m)}+\mu_T^{(m)}}\right)^2+\left(\frac{\sigma_{r\theta}^{(f)}(S_{0k})-t_t(S_{0k})}{2\mu_T^{(m)}}\right)^2\right.\\ \left.+\left(\frac{\sigma_{rr}^{(m)}(S_{0k})-t_n(S_{0k})}{k_T^{(m)}+\mu_T^{(m)}}\right)^2+\left(\frac{\sigma_{r\theta}^{(m)}(S_{0k})-t_t(S_{0k})}{2\mu_T^{(m)}}\right)^2\right]\\ +\frac{1}{N_0}\sum_{k=1}^{k=N_0}\gamma_{0k}^{u}\left[\left(u_r'^{(f)}(S_{0k})-u_r'^{(m)}(S_{0k})-\Delta u_n\right)^2\right]\end{aligned} \tag{39}$$

for out-of-plane loading:

$$\mathcal{L}_{S_0} = \frac{1}{N_0}\sum_{k=1}^{k=N_0}\gamma_{0k}^{\sigma}\left[\left(\frac{\sigma_{zr}^{(f)}(S_{0k})-t_t(S_{0k})}{\mu_T^{(m)}}\right)^2+\left(\frac{\sigma_{zr}^{(m)}(S_{0k})-t_t(S_{0k})}{\mu_T^{(m)}}\right)^2\right] \tag{40}$$

This straightforward way of implementing the cohesive interface model stands in contrast to the elasticity-based approaches, where only a constant interfacial stiffness can be applied at every angular position. It is also in contrast with the finite-element-based implementation, wherein significant stiffness is utilized within the interfacial traction-separation law under compressive conditions.

Table 2 Cohesive interface parameters

Parameters	σ_0(MPa)	$\Delta u_0(\mu m)$	σ_1(MPa)	$\Delta u_1(\mu m)$
Values	40	0.04	15	0.015

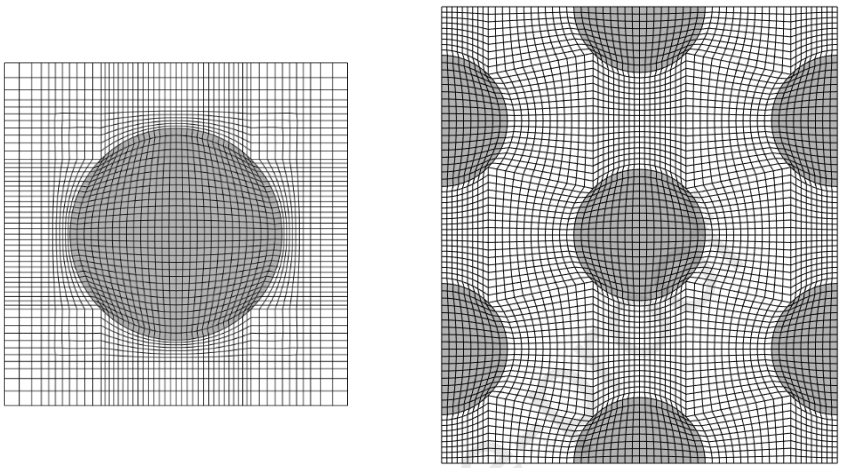

(a) Square array (b) Hexagonal array

Figure 14 Unit cell discretization in FVDAM analysis

We consider hexagonal and square arrays with 30% fiber volume fraction, with interface parameters listed in Table 2. The fiber has a radius of $1\mu m$. For direct comparison with the FHN model, we employ the finite-volume direct averaging micromechanics model (FVDAM) with the cohesive zone model developed by Tu and Pindera (2016; 2014) and Tu and Chen (2020a, b). It should be noted that the FVDAM with CZM capability necessitates the use of row-wise and column-wise mesh discretization, as shown in Figure 14. Therefore, for the hexagonal periodic array of fibers, a multi-inclusion unit cell needs to be considered. Figure 15(a) illustrates the comparison of normal and tangential stresses σ_{rr} and $\sigma_{r\theta}$ as a function of angular position on the interface, for both square and hexagonal arrays, under biaxial loading $\overline{\varepsilon}_{22} = -2\overline{\varepsilon}_{33} = 1\%$. Figure 14(b) shows the comparison of normal and tangential displacement discontinuities $\Delta u_r'$ and $\Delta u_t'$ distributions across the interface for both arrays. Thorough scrutiny of the interfacial stresses and

displacements unveils excellent correlations between the FHN and FVDAM results. Distinctions between the square and hexagonal arrays arise from the interactions among the fibers. Figure 16 and 17 compare the FHN prediction of local stress field σ_{22}, σ_{33} and σ_{23} distributions against the FVDAM results for the square and hexagonal arrays of fibers, respectively. It is noted that the load-bearing capacity of the fibers diminishes as a result of interface decohesion. The significant stress concentration within the fiber phase in the shear stress component distinctly signifies the opening of cracks around the fiber.

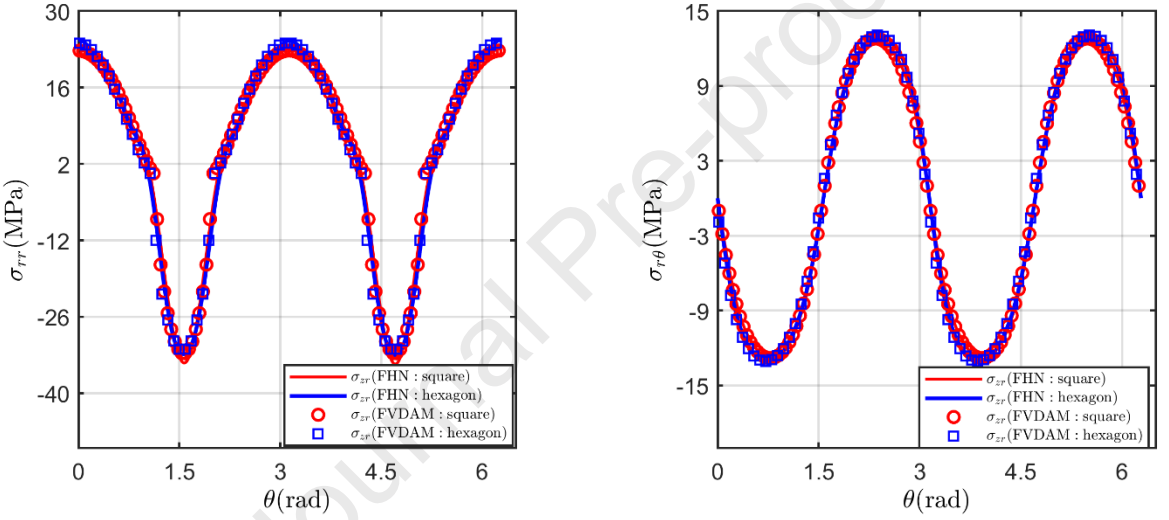

(a)

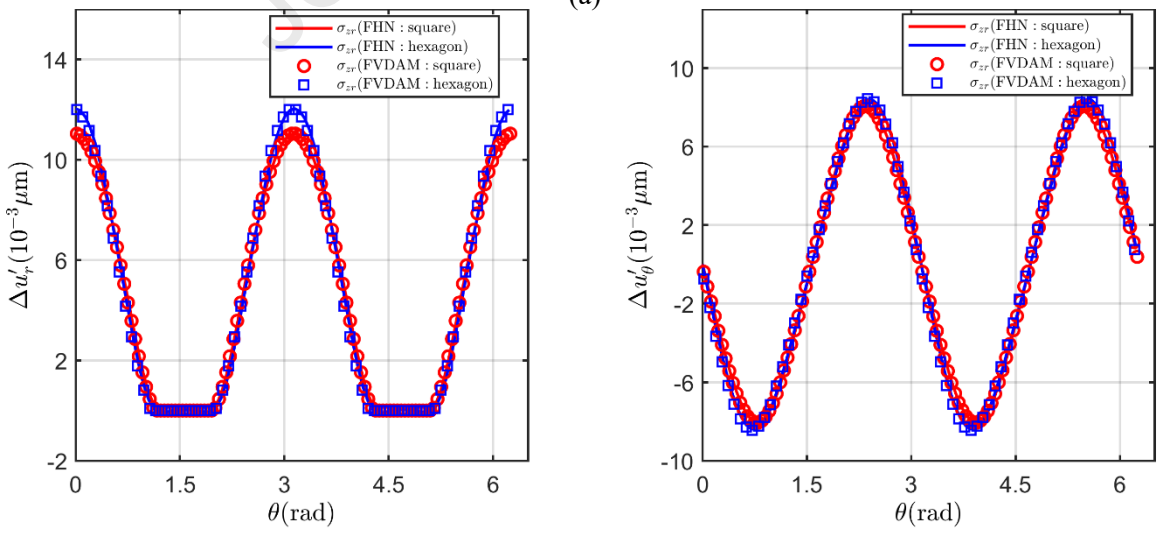

(b)

Figure 15 (a) Interfacial radial and tangential stress distributions; (b) Interfacial radial and tangential displacement discontinuities distributions. Comparison of the square and hexagonal arrays of fibers undergoing interfacial debonding under biaxial strain loading $\bar{\varepsilon}_{22} = -2\bar{\varepsilon}_{33} = 1\%$. It is noted that when the interface is under compressive radial stress, the radial displacement discontinuities are eliminated in the prediction

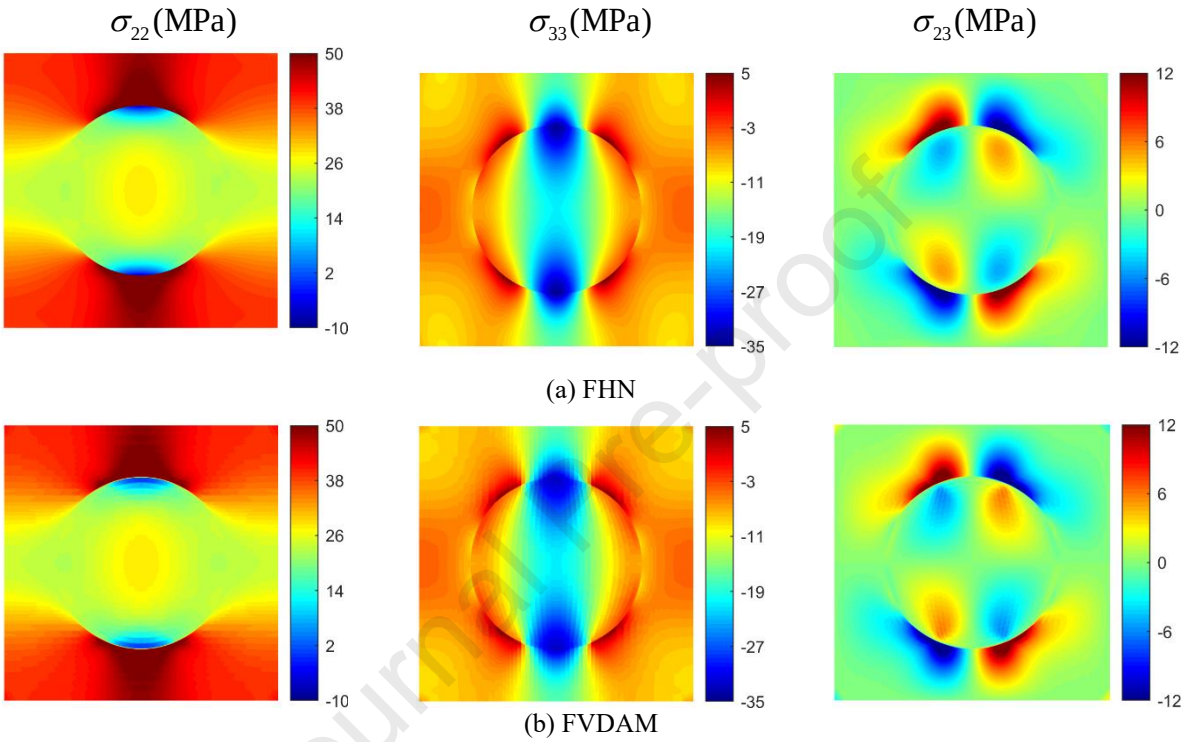

Figure 16 Selected local stress field σ_{22} , σ_{33} , σ_{23} distributions under biaxial strain loading $\bar{\varepsilon}_{22} = -2\bar{\varepsilon}_{33} = 1\%$. Comparison of FHN prediction with FVDAM technique for square arrays of fibers undergoing interfacial debonding.

In the last numerical experiment, the unit cells are subjected to biaxial shear loading $\bar{\varepsilon}_{12} = 2\bar{\varepsilon}_{13} = 1\%$. Comparison of interfacial axial shear stress σ_{zr} and displacement discontinuity u_z' generated by the FHN and FVDAM approaches is presented in Figure 18. Under axial shear loading, the hexagonal and square arrays predict nearly identical results, indicating the fiber-fiber interaction is negligible at this volume content. Figures 19 and 20 show comparison of local stress

σ_{12} and σ_{13} distributions within the unit cell microstructures generated by the FHN and FVDAM for square and hexagonal arrays, respectively. Once more, the FHN demonstrates an excellent correlation with the FVDAM results. The occurrence of interface debonding contributes to the diminishment of the load-bearing capacity within the fiber phase.

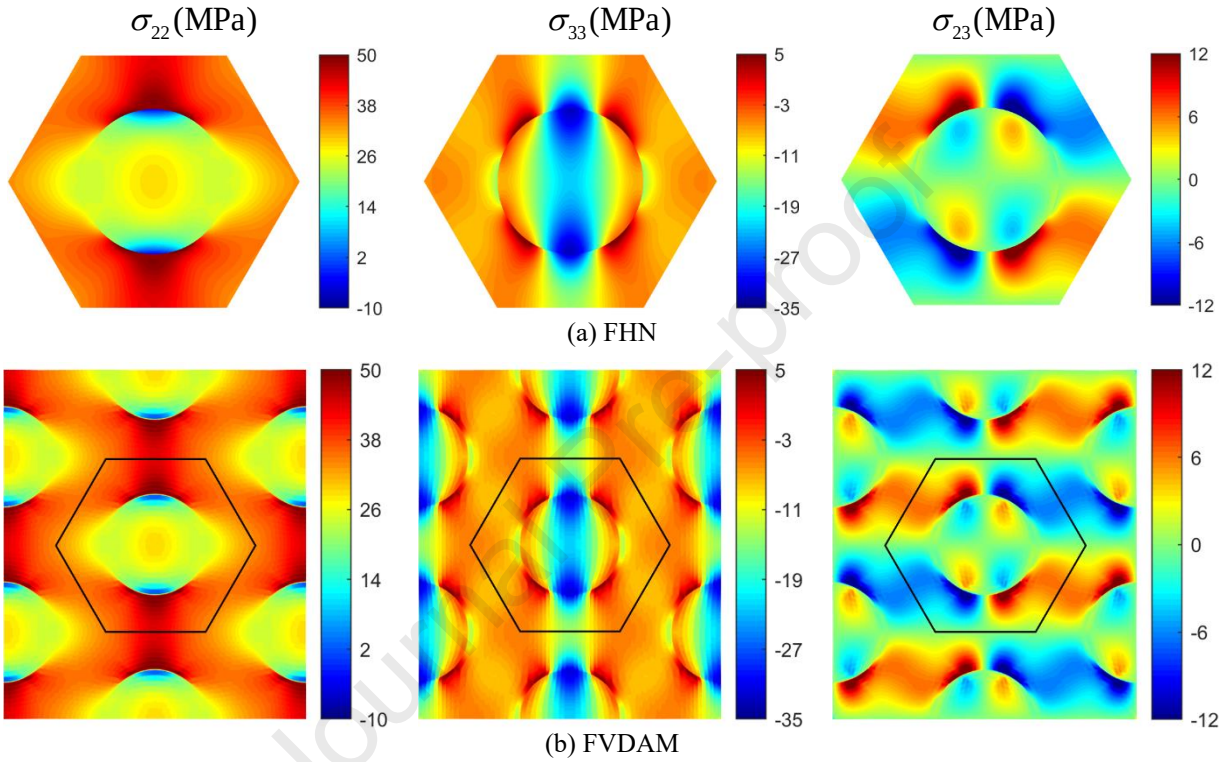

Figure 17 Selected local stress field σ_{22} , σ_{33} , σ_{23} distributions under biaxial strain loading $\bar{\varepsilon}_{22} = -2\bar{\varepsilon}_{33} = 1\%$. Comparison of FHN prediction with FVDAM technique for hexagonal arrays of fibers undergoing interfacial debonding.

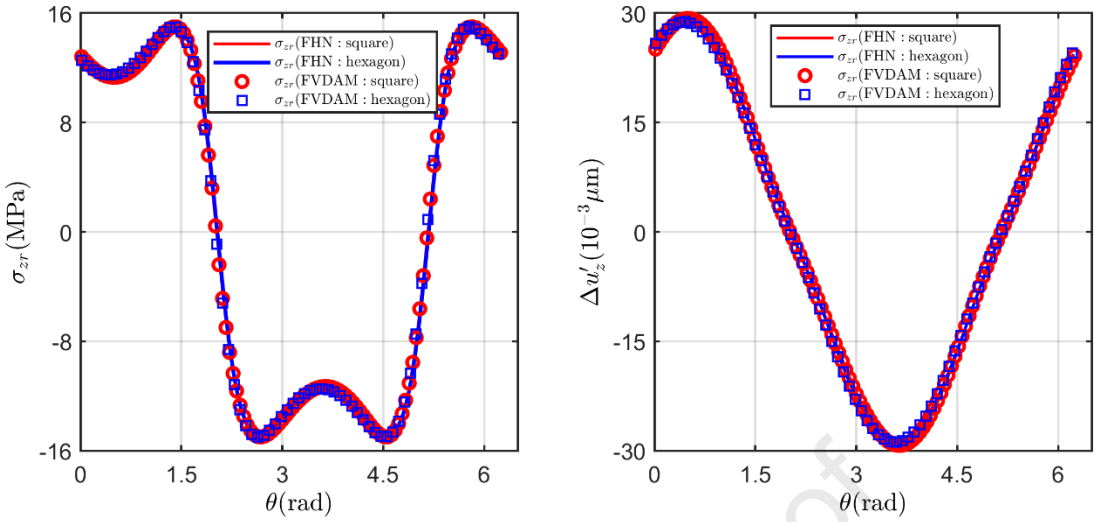

(a) (b)

Figure 18 (a) Anti-plane interfacial tangential stress distributions; (b) Interfacial axial displacement discontinuities distributions. Comparison of FHN predictions with FVDAM techniques for square and hexagonal arrays of fibers undergoing interfacial debonding under biaxial strain loading $\overline{\varepsilon}_{12} = 2\overline{\varepsilon}_{13} = 1\%$

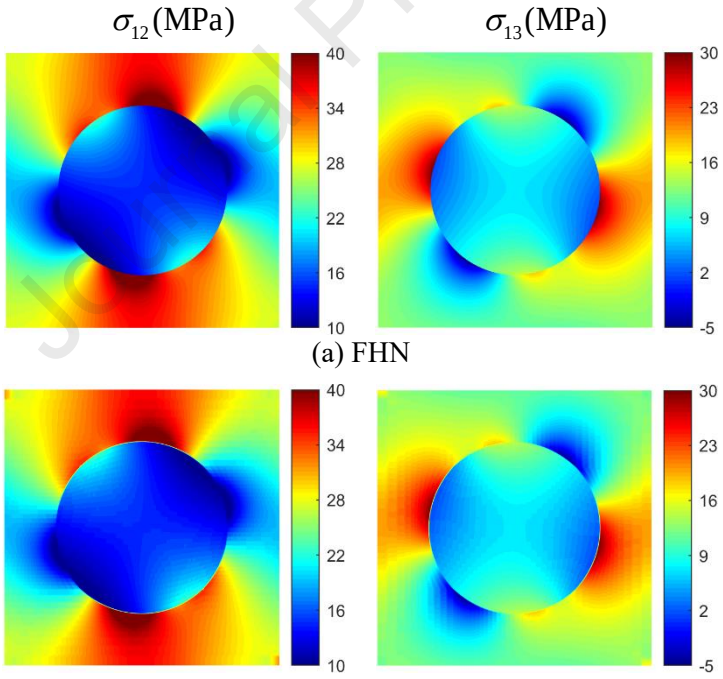

(a) FHN

(b) FVDAM

Figure 19 Local stress field σ_{12} , σ_{13} distributions under biaxial strain loading $\overline{\varepsilon}_{12} = 2\overline{\varepsilon}_{13} = 1\%$. Comparison of FHN prediction with FVDAM technique for square arrays of fibers undergoing interfacial debonding.

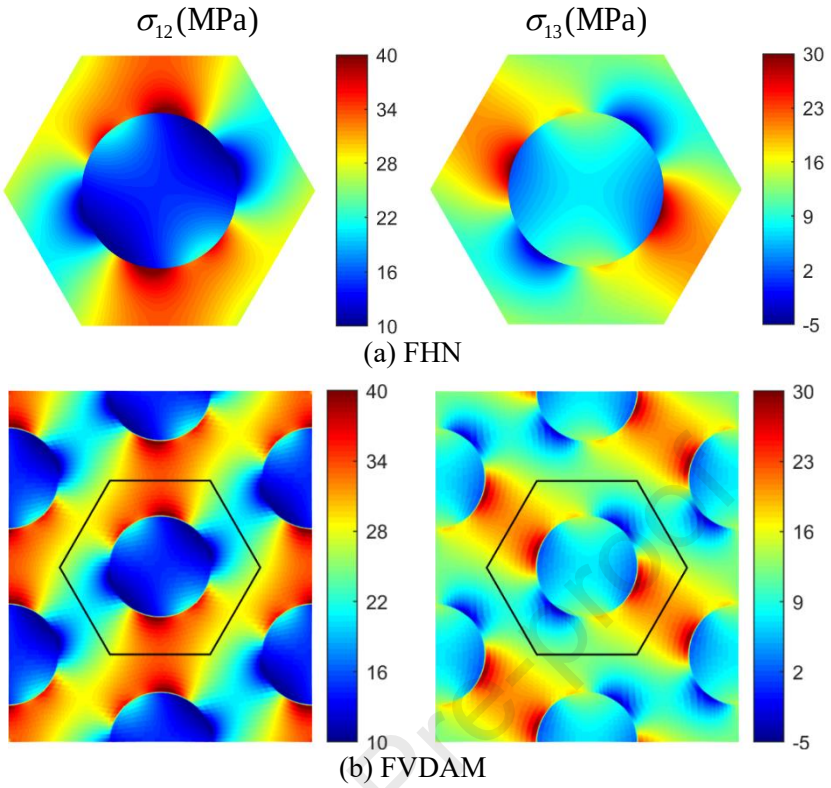

Figure 20 Local stress field σ_{12} , σ_{13} distributions under biaxial strain loading $\bar{\varepsilon}_{12} = 2\bar{\varepsilon}_{13} = 1\%$ Comparison of FHN prediction with FVDAM technique for hexagonal array of fibers undergoing interfacial debonding

7. Summary and Conclusions

A novel physically informed machine learning framework has been proposed to predict displacement and stress fields in microstructured materials with periodic distributions of unidirectional fibers. In the theory of elasticity, the Fourier series solutions to Navier's displacement differential equations were exploited to form network models for the fiber and matrix phases, respectively. The network loss function was constructed as mean square differences of traction and displacement at the fiber/matrix interface as well as at the exterior mirrored faces of repeating unit cells, evaluated over a set of weighted collocation points. The automatic differentiation was exploited to construct the loss function, which significantly simplifies setting up the network model. To alleviate the adverse competition of multiple loss terms, the collocation

point weights were trained concurrently with the network parameters. We also demonstrate that the transfer learning technique can be explored to speed up the training of new geometries after a similar model has already been trained. The predictive capabilities of the FHN model were demonstrated upon comparison with the finite-element unit cell solutions for several microstructural configurations and loading conditions.

The incorporation of a cohesive zone interface model within the FHN framework, verified against comparison with the finite-volume based technique, provides an additional novelty to the present manuscript. The interfacial normal and tangential tractions and displacements can be directly evaluated at each collocation point, allowing straightforward incorporation of arbitrary interfacial traction-separation relations. It stands in contrast to the elasticity-based solutions, wherein only the spring interface with constant interfacial stiffness at all angular positions can be applied. Additionally, when a collocation point on the interface is under compressive normal stress, the normal displacement discontinuity can be directly set to zero at the associated collocation points to avoid material interpenetration. The latter offers a distinct advantage relative to the finite-element-based cohesive interface implementation that requires a high interfacial stiffness within the interfacial traction-separation law under compressive conditions.

Despite challenges in computational efficiency, the proposed method offers several distinct advantages relative to the classical approaches such as FEM. For instance, the FHN framework ensures the local satisfaction of the stress equilibrium equations while the traditional FEM enforces equilibrium in an approximate fashion with sufficient mesh refinement. Moreover, the FHN-generated displacements are infinitely differentiable. Hence the predicted stresses are continuous and smoothly varying in the fiber and matrix domains. Conversely, the FEM can only fullfill C^0 continuity of displacements while the calculated stresses are not necessarily continuous from one

element to another. Lastly, the proposed FHN homogenization method is a mesh-free technique, requiring only interface collocation points to formulate the loss function. The construction of the input file in FHN is much simpler than the FEM-based homogenization method. Thus, the proposed FHN framework has a valuable role in micromechanics theories and shows promise for further development.

Acknowledgment

Dr. Zhibo Yang gratefully acknowledges the financial support of the National Natural Science Foundation of China (Nos. 52222504 and 52241502).

References

Barenblatt, G.I., 1959. The formation of equilibrium cracks during brittle fracture. General ideas and hypotheses. Axially-symmetric cracks. Journal of applied mathematics and mechanics 23, 622-636.

Camacho, G.T., Ortiz, M., 1996. Computational modelling of impact damage in brittle materials. International Journal of Solids and Structures 33, 2899-2938.

Cavalcante, M.A., Pindera, M.-J., 2016. Generalized FVDAM theory for elastic–plastic periodic materials. International Journal of Plasticity 77, 90-117.

Chatzigeorgiou, G., Charalambakis, N., Chemisky, Y., Meraghni, F., 2018. 1 - Mathematical Concepts, in: Chatzigeorgiou, G., Charalambakis, N., Chemisky, Y., Meraghni, F. (Eds.), Thermomechanical Behavior of Dissipative Composite Materials. Elsevier, pp. 1-36.

Chen, Q., Chatzigeorgiou, G., Meraghni, F., Javili, A., 2022. Homogenization of size-dependent multiphysics behavior of nanostructured piezoelectric composites with energetic surfaces. European Journal of Mechanics - A/Solids 96, 104731.

Chen, Q., Wang, G., Pindera, M.-J., 2018. Homogenization and localization of nanoporous composites - A critical review and new developments. Composites Part B: Engineering 155, 329-368.

Chen, Q., Xiao, C., Yang, Z., Tabet, J., Chen, X., 2024. Deep neural network homogenization of multiphysics behavior for periodic piezoelectric composites. Composites Part A: Applied Science and Manufacturing, 108421.

Christensen, R., Lo, K., 1979. Solutions for effective shear properties in three phase sphere and cylinder models. Journal of the Mechanics and Physics of Solids 27, 315-330.

Cruz-González, O.L., Rodríguez-Ramos, R., Otero, J.A., Ramírez-Torres, A., Penta, R., Lebon, F., 2020. On the effective behavior of viscoelastic composites in three dimensions. International Journal of Engineering Science 157, 103377.

Dong, S., Ni, N., 2021. A method for representing periodic functions and enforcing exactly periodic boundary conditions with deep neural networks. Journal of Computational Physics 435, 110242.

Drago, A., Pindera, M.J., 2007. Micro-macromechanical analysis of heterogeneous materials: Macroscopically homogeneous vs periodic microstructures. Composites Science and Technology 67, 1243-1263.

Drago, A.S., Pindera, M.-J., 2008. A Locally Exact Homogenization Theory for Periodic Microstructures With Isotropic Phases. Journal of Applied Mechanics 75.

Du, X., Chen, Q., Chatzigeorgiou, G., Meraghni, F., Zhao, G., Chen, X., 2024. Nitsche's Method Enhanced Isogeometric Homogenization of Unidirectional Composites with Cylindrically Orthotropic Carbon/Graphite Fibers. Composites Science and Technology 256, 110787.

Dugdale, D.S., 1960. Yielding of steel sheets containing slits. Journal of the Mechanics and Physics of Solids 8, 100-104.

El Fallaki Idrissi, M., Praud, F., Meraghni, F., Chinesta, F., Chatzigeorgiou, G., 2024. Multiscale Thermodynamics-Informed Neural Networks (MuTINN) towards fast and frugal inelastic computation of woven composite structures. Journal of the Mechanics and Physics of Solids 186, 105604.

Haghighat, E., Raissi, M., Moure, A., Gomez, H., Juanes, R., 2021. A physics-informed deep learning framework for inversion and surrogate modeling in solid mechanics. Computer Methods in Applied Mechanics and Engineering 379, 113741.

Hashin, Z., Rosen, B.W., 1964. The Elastic Moduli of Fiber-Reinforced Materials. Journal of Applied Mechanics 31, 223-232.

He, Z., Pindera, M.-J., 2020. Locally exact asymptotic homogenization of periodic materials under anti-plane shear loading. European Journal of Mechanics - A/Solids 81, 103972.

Henkes, A., Wessels, H., Mahnken, R., 2022. Physics informed neural networks for continuum micromechanics. Computer Methods in Applied Mechanics and Engineering 393, 114790.

Huang, S., He, Z., Chem, B., Reina, C., 2022. Variational Onsager Neural Networks (VONNs): A thermodynamics-based variational learning strategy for non-equilibrium PDEs. Journal of the Mechanics and Physics of Solids 163, 104856.

Jiang, J., Wu, J., Chen, Q., Chatzigeorgiou, G., Meraghni, F., 2023. Physically informed deep homogenization neural network for unidirectional multiphase/multi-inclusion thermoconductive composites. Computer Methods in Applied Mechanics and Engineering 409, 115972.

McClenny, L.D., Braga-Neto, U.M., 2023. Self-adaptive physics-informed neural networks. Journal of Computational Physics 474, 111722.

Mori, T., Tanaka, K., 1973. Average stress in matrix and average elastic energy of materials with misfitting inclusions. Acta Metallurgica 21, 571-574.

Needleman, A., 1987. A Continuum Model for Void Nucleation by Inclusion Debonding. Journal of Applied Mechanics 54, 525-531.

Ortiz, M., Suresh, S., 1993. Statistical Properties of Residual Stresses and Intergranular Fracture in Ceramic Materials. Journal of Applied Mechanics 60, 77-84.

Pindera, M.-J., Khatam, H., Drago, A.S., Bansal, Y., 2009. Micromechanics of spatially uniform heterogeneous media: a critical review and emerging approaches. Composites Part B: Engineering 40, 349-378.

Praud, F., Chatzigeorgiou, G., Meraghni, F., 2020. Fully integrated multi-scale modelling of damage and time-dependency in thermoplastic-based woven composites. International Journal of Damage Mechanics 30, 163-195.

Raissi, M., Perdikaris, P., Karniadakis, G.E., 2019. Physics-informed neural networks: A deep learning framework for solving forward and inverse problems involving nonlinear partial differential equations. Journal of Computational Physics 378, 686-707.

Samaniego, E., Anitescu, C., Goswami, S., Nguyen-Thanh, V.M., Guo, H., Hamdia, K., Zhuang, X., Rabczuk, T., 2020. An energy approach to the solution of partial differential equations in computational mechanics via machine learning: Concepts, implementation and applications. Computer Methods in Applied Mechanics and Engineering 362, 112790.

Tu, W., Chen, Q., 2020a. Evolution of interfacial debonding of a unidirectional graphite/polyimide composite under off-axis loading. Engineering Fracture Mechanics 230, 106947.

Tu, W., Chen, Q., 2020b. Homogenization and localization of unidirectional fiber-reinforced composites with evolving damage by FVDAM and FEM approaches: A critical assessment. Engineering Fracture Mechanics 239, 107280.

Tu, W., Pindera, M.-J., 2016. Damage evolution in cross-ply laminates revisited via cohesive zone model and finite-volume homogenization. Composites Part B: Engineering 86, 40-60.

Tu, W.Q., Pindera, M.J., 2014. Cohesive Zone-Based Damage Evolution in Periodic Materials Via Finite-Volume Homogenization. Journal of Applied Mechanics-Transactions of the Asme 81, 101005.

Vahab, M., Haghighat, E., Khaleghi, M., Khalili, N., 2022. A Physics-Informed Neural Network Approach to Solution and Identification of Biharmonic Equations of Elasticity. Journal of Engineering Mechanics 148, 04021154.

Wang, G., Pindera, M.-J., 2016. Locally-exact homogenization theory for transversely isotropic unidirectional composites. Mechanics Research Communications 78, 2-14.

Wu, J., Chen, Q., Jiang, J., Chatzigeorgiou, G., Meraghni, F., 2024. Adaptive deep homogenization theory for periodic heterogeneous materials. Composite Structures 340, 118171.

Wu, J., Jiang, J., Chen, Q., Chatzigeorgiou, G., Meraghni, F., 2023. Deep homogenization networks for elastic heterogeneous materials with two- and three-dimensional periodicity. International Journal of Solids and Structures 284, 112521.

Xu, X.P., Needleman, A., 1994. Numerical simulations of fast crack growth in brittle solids. Journal of the Mechanics and Physics of Solids 42, 1397-1434.

Highlights

- An elasticity-inspired machine learning approach is developed for the homogenization of composites
- Boundary conditions are implemented using the collocation method
- A cohesive zone model is incorporated to simulate interfacial damage
- Comparison with finite element/volume-based solutions showcases the computational capability of the proposed method

Declaration of interests

☒ The authors declare that they have no known competing financial interests or personal relationships that could have appeared to influence the work reported in this paper.

☐ The authors declare the following financial interests/personal relationships which may be considered as potential competing interests: